Sensitivity of the marine biospheric Si cycle for biogeochemical parameter variations

C. Heinze, A. Hupe, and E. Maier-Reimer
Max Planck Institute of Meteorology, Hamburg, Germany

N. Dittert and O. Ragueneau
Unité Mixte de Recherche 6539-IUEM, Plouzané, France

Received 10 June 2002; revised 18 December 2002; accepted 8 April 2003; published 6 September 2003.

[1] A systematic quantitative assessment of the marine silicon cycle is presented, based on a prognostic coupled water column-sediment global biogeochemical ocean general circulation model (HAMOCC). The resulting tracer distributions are compared with a comprehensive marine Si database of measurements. The model parameters which govern the Si cycle within the model world are optimized through a linear response model. The functional relationships between the Si cycle parameters and the Si tracer distributions are derived from a series of sensitivity experiments addressing opal export production, particle flux through the water column, porewater chemistry, and external biogeochemical forcing. The most important parameters for a further quantitative improvement of the simulation are depth-dependent opal dissolution kinetics, a productivity-dependent opal settling velocity, a general change in maximum Si uptake velocity V_{max}^{opal}, and the clay as well as the Si input from continental weathering. The modeled Si budget shows a larger global export production, larger opal deposition rates onto the sediment surface and higher diffusive transports of porewater silicic acid into the open water column as estimated by *Tréguer et al.* [1995]. *INDEX TERMS:* 1050 Geochemistry: Marine geochemistry (4835, 4850); 4842 Oceanography: Biological and Chemical: Modeling; 4835 Oceanography: Biological and Chemical: Inorganic marine chemistry; *KEYWORDS:* marine biogeochemistry, ocean modeling, silicon cycle, model optimization, opal sediment, early diagenesis

Citation: Heinze, C., A. Hupe, E. Maier-Reimer, N. Dittert, and O. Ragueneau, Sensitivity of the marine biospheric Si cycle for biogeochemical parameter variations, *Global Biogeochem. Cycles,* , *17*(3), 1086, doi:10.1029/2002GB001943, 2003.

1. Introduction

[2] The oceanic biogeochemical silicon cycle serves as the interface between input of silicic acid $Si(OH)_4$ from terrestrial sources and output of biogenic silica ($BSiO_2$ or opal) through accumulation of sediment. The principal redistribution pathways and global bulk numbers for marine Si fluxes are fairly well established [*DeMaster*, 1981; *Tréguer et al.*, 1995; *Nelson et al.*, 1995]. Besides the cycling of $BSiO_2$, silicon enters the ocean also in particulate form as a weathering product of the continental crust. This fairly inert quartz and alumino-silicate component is not the focus of the present study.

[3] Silicon in the ocean is of relevance for several reasons. A major part of the oceanic biogenic particle export production is driven by siliceous phytoplankton (diatoms) consisting of rather large and fast-sinking aggregates [*Dugdale et al.*, 1995; *Buesseler*, 1998]. In some regions of the ocean Si is assumed to be a biolimiting nutrient [*Dugdale and Wilkerson*, 1998]. Besides this ecological significance, the percentage of opal in the sediment is potentially a valuable quantitative paleo climate tracer [*Ragueneau et al.*, 1996] which reflects paleo productivity and hence ocean circulation as well as upwelling strength. The straightforward use of opal as a paleo tracer is hampered by the limited knowledge about the factors influencing the regionally varying opal deposits [*Ragueneau et al.*, 2000].

[4] The advancement in modeling global biogeochemical cycles with three-dimensional general circulation models and the availability of silicon data from all marine reservoirs make it intriguing to attempt a new quantitative estimate of the global marine silicon cycle. This attempt is made here with the help of the HAMOCC model, a newly compiled comprehensive marine silicon database, and a systematic optimization procedure.

2. Model Description

[5] We employ the Hamburg oceanic carbon cycle model (HAMOCC, originally developed by *Maier-Reimer* [1993]) in its annually averaged version including interactive sediment [*Heinze et al.*, 1999; *Heinze and Maier-Reimer*, 1999] and a representation of the marine biogeochemical silicon cycle. The model is based on the three-dimensional fields

0886-6236/03/2002GB001943

of velocity components, potential temperature, salinity, and convective mixing as provided by the dynamical Large-Scale Geostrophic Ocean General Circulation Model (LSG-OGCM [*Maier-Reimer et al.*, 1993]). In this study, the most efficient model version with respect to CPU time is used, i.e., with a horizontal resolution of $3.5^\circ \times 3.5^\circ$ and 11 layers (centered at 25, 75, 150, 250, 450, 700, 1000, 2000, 3000, 4000, and 5000 m) in order to be able to run the model repeatedly into full equilibrium including the bioturbated sediment zone. The model has a smoothed realistic topography. The velocity field which is taken from *Winguth et al.* [1999] represents the preindustrial ocean. Climatological forcing fields were used for this velocity field (monthly mean windstress data from the atmospheric circulation model version 3 of the European Center for Medium-Range Weather Forecast, with special modifications for climate studies made by several groups at Hamburg with a truncation of the wave spectrum at wavenumber 42 or the so-called ECHAM3/T42 model [*Lorenz et al.*, 1996]; monthly averaged air temperatures from the Comprehensive Ocean Atmosphere Data Set (COADS) [*Woodruff et al.*, 1987]; and climatological annually averaged surface salinities after *Levitus* [1982]). The LSG-OGCM also includes a simple sea ice model to account for brine release during freezing. Details concerning the physical model are given by *Winguth et al.* [1999]. The physical model results were averaged over 1 year for use in the annually averaged biogeochemical model.

[6] For any realistic simulation of oceanic biogeochemical tracer fields, an appropriate three-dimensional velocity field is essential. Here we had to make a compromise between spatial as well as temporal model resolution and computational efficiency. The fairly coarse vertical resolution of the model in the deep ocean necessarily leads to a smoothing and somewhat too weak gradients in simulated distributions as compared to a corresponding model with a twice as high vertical resolution. As compared to our 11-layer version here, a corresponding 22-layer model of the same type can reproduce the natural radiocarbon especially in the North Pacific better. The differences in the representation of near-surface processes, including the equatorial upwelling, between the two configurations are small. The 22-layer LSG-OGCM was compared with a series of other cutting edge coarse resolution OGCMs in a comprehensive intercomparison study also with respect to the simulation of radiocarbon [*Orr*, 2001]. As compared to these models, the annually averaged 11-layer version of the Large-Scale Geostrophic model flow field as applied in our study is still well competitive if fast model integrations are required (see simulations of a broad variety of geochemical tracers including, radiocarbon, $\delta^{13}C$, oxygen, phosphate, oxygen, $CaCO_3$ sediment, and particle reactive metals [e.g., *Archer and Maier-Reimer*, 1994; *Winguth et al.*, 1999; *Heinze et al.*, 1999; *Henderson et al.*, 1999; *Heinze*, 2001, 2002a, 2002b; *Gehlen et al.*, 2003]).

[7] The biogeochemical model includes the three reservoirs: atmosphere, ocean, and bioturbated sediment. The atmosphere is considered well mixed zonally, while meridional troposheric tracer transport is represented through diffusion. The total thickness of the bioturbated sediment is set to 10 cm. Ten layers with increasing thickness subdivide the sediment (layers centered at 0.3, 0.45, 1.35, 1.85, 2.6, 3.6, 4.6, 6.325, and 8.775 cm). The porosity decreases from 0.95 at the uppermost sediment layer to 0.75 at the base of the bioturbated zone following *Ullman and Aller* [1982]. Prognostic tracer variables are in the atmosphere carbon dioxide and oxygen, in the water column total alkalinity (TAlk), total CO_2 (TCO_2, equivalent to dissolved inorganic carbon, DIC), phosphate, oxygen, dissolved organic carbon (DOC) and silicic acid, in the sediment porewaters the same tracers as in the water column (except for DOC), and in the solid sediment calcium carbonate, opal, organic carbon, and clay. The model is initialized from homogeneous distributions in the atmosphere and water column and from clay throughout the bioturbated sediment. During the integration, the model builds up its own biogenic sediment. Integrations usually run at least over several ten thousands of years.

[8] Input of silicic acid, phosphate, oxygen, DIC, TAlk, and clay from continental weathering is prescribed as a constant flux homogeneously over the ocean to account for the loss through sediment accumulation of organic carbon, $CaCO_3$, opal and clay. When the simulated tracer distributions approach equilibrium, the global sediment accumulation rates approach asymptotically the prescribed weathering input fluxes. Continental margin processes are not explicitly simulated in this coarse resolution study. In the standard case a throughput rate of 5.5×10^{12} mol Si yr^{-1} was used. This value corresponds to the total river input plus aeolian deposition of Si to the ocean minus the Si deposits on shallow shelf systems according to *Tréguer et al.* [1995]. Fluxes from hydrothermal vents and basalt into the deep sea as well as ground water seeping from land were neglected here as they are comparatively small. Recent modifications of the model (with respect to *Heinze et al.* [1999] and *Heinze and Maier-Reimer* [1999]) are described in the following paragraphs.

2.1. Export Production of Biogenic Particles

[9] In the annually averaged model, for biological particle production, only export production is modeled. Phosphate serves as biolimiting nutrient. Particle production takes place in the model surface layer (thickness 50 m) representing the euphotic zone. Both POC (particulate organic carbon) and opal export productions are simulated through Michaelis Menten nutrient uptake kinetics [e.g., *Parsons and Takahashi*, 1973],

$$P_{POC} = \frac{V_{max}^{POC} \cdot \left[PO_4^{3-}\right]^2 \cdot Red(C:P)}{K_s^{POC} + \left[PO_4^{3-}\right]} \tag{1}$$

$$P_{opal} = \frac{V_{max}^{opal} \cdot \left[Si(OH)_4\right]^2}{K_s^{opal} + \left[Si(OH)_4\right]}, \tag{2}$$

where

P_{POC} POC export production (mol L^{-1} yr^{-1});
$Red(C:P)$ Redfield ratio C:P;
V_{max}^{POC} maximum uptake rate of phosphate (yr^{-1});
K_s^{POC} half saturation constant for POC production (mol L^{-1});

P_{opal} opal export production (mol L^{-1} yr^{-1});
V_{max}^{opal} maximum uptake rate of silicic acid (yr^{-1});
K_s^{opal} half saturation constant for opal production (mol L^{-1}).

In contrast to earlier versions of the annually averaged biogeochemical model parameters V_{max}^{POC}, V_{max}^{opal}, K_s^{POC}, and K_s^{opal} are scaled with sea surface temperature. For V_{max}^{POC} the following formulation is applied:

$$V_{max}^{POC} = C_{V1} + SST \cdot \frac{C_{V2}}{T_{max} - T_{min}}, \tag{3}$$

where SST is the sea surface temperature in °C and T_{max} and T_{min} are upper and lower temperature cutoff values (set to 25 and 0.1°C). C_{V1} and C_{V2} are adjustable constants set to 0.3 yr^{-1} and 0.7 yr^{-1}, respectively. V_{max}^{opal} is set to $V_{max}^{POC} \times 2.5$. These values resulted in a reasonable pattern of annual export production rates when compared to estimated values based on observations [e.g., *Berger et al.*, 1987]. A systematic choice of these parameters on the basis of observations is difficult for a global coarse resolution model with a large time step. Observational evidence on temperature dependencies of V_{max}^{POC} is contradictory, only regionally valid, and probably also time dependent [see, e.g., *Behrenfeld and Falkowski*, 1997, Figure 4]. In order to test the validity of the V_{max}^{opal} value, a sensitivity experiment for this parameter was carried out (see paragraph on optimization below). For the half saturation constants an expression is used which accounts mainly for an increase of the K_s values at low temperatures (in order to increase the preformed nutrient values somewhat in high latitudes),

$$K_s = K_{max} - (K_{max} - K_{min}) \cdot \frac{F_K}{C_{K1} + F_K}$$
$$F_K = e^{C_{K2} \cdot SST - C_{K3}}. \tag{4}$$

The values for the constants K_{max} and K_{min} are set to 0.17 μmol/L and 0.05 μmol/L for phosphate and to 10.0 μmol/L and 3.0 μmol/L for silicic acid following estimates from observations (*Thomas and Dodson* [1968] for P; *Paasche* [1973], and *Goering et al.* [1973] for Si). For C_{K1}, C_{K2}, and C_{K3}, values of 5.0, 1.0, and 3.0 are used throughout. These parameters were chosen so that a reasonable first approximation for the water column silicic acid concentrations was achieved. Alternative formulations of the K_s for silicon uptake were investigated during the model optimization (see below). Iron limitation and fertilization was not considered in the control run of the model but was considered for the model optimization.

2.2. Particle Flux Through the Water Column

[10] In earlier models, the redistribution of biogenic particles leaving the euphotic zone as export production was performed with a prescribed redistribution profile [e.g., *Maier-Reimer*, 1993; *Heinze et al.*, 1991; *Najjar et al.*, 1992] through an exponential or hyperbolic function [*Volk and Hoffert*, 1985; *Martin et al.*, 1987; *Suess*, 1980]. These profile functions include in one characteristic coefficient the effects of both the particle settling velocity and the particle dissolution rate constant. We aim here at discriminating between these two effects. In order to enable explicit choice of the sinking velocity and the dissolution rate constants at each grid point, additional variables are introduced, named POC_{settle}, $CaCO_{3settle}$, and $opal_{settle}$. These variables are the instantaneous particle concentrations of sinking matter at each grid box. The balance equation for $opal_{settle}$ is

$$\frac{d\ opal_{settle}}{dt} = gain - loss$$
$$\frac{d\ opal_{settle}}{dt} = P_{opal} - \frac{w_{opal}}{\Delta z_0} \cdot opal_{settle} - r_{opal} \cdot opal_{settle} \qquad (surface\ layer)$$
$$\frac{d\ opal_{settle}}{dt} = w_{opal} \cdot \frac{\partial opal_{settle}}{\partial z} - r_{opal} \cdot opal_{settle} \qquad (other\ layers), \tag{5}$$

where w_{opal} is the particle settling velocity for opal (m yr^{-1}), r_{opal} is the reaction rate (yr^{-1}) constant for degradation of opal, and Δz_0 is the thickness of the euphotic zone (m). The implicit numerical scheme for this formulation is directly solvable,

$$opal_{settle,1}^{new} - opal_{settle,1}^{old} = P_{opal} - w_{opal} \cdot \frac{\Delta t}{\Delta z_1} \cdot opal_{settle,1}^{new} - r_{opal} \cdot \Delta t \cdot opal_{settle,1}^{new}$$
$$opal_{settle,k}^{new} - opal_{settle,k}^{old} = w_{opal} \cdot \frac{\Delta t}{\Delta z_k} \cdot opal_{settle,k-1}^{new} - w_{opal} \cdot \frac{\Delta t}{\Delta z_k} \cdot opal_{settle,k}^{new} - r_{opal} \cdot \Delta t \cdot opal_{settle,k}^{new}, \tag{6}$$

where

$opal_{settle,1}^{new}$ concentration of sinking opal in surface layer, new time level (mol L^{-1});
$opal_{settle,1}^{old}$ concentration of sinking opal in surface layer, old time level (mol L^{-1});
$opal_{settle,k}^{new}$ concentration of sinking opal in layer k, new time level (mol L^{-1}) k > 1;
$opal_{settle,k}^{old}$ concentration of sinking opal in layer k, old time level (mol L^{-1}) k > 1;
$opal_{settle,k-1}^{new}$ concentration of sinking opal in layer above layer k, new time level (mol L^{-1}) k > 1;
Δz_k thickness of layer k (m).

Corresponding expressions are applied for suspended $CaCO_{3settle}$ and POC_{settle} using separate values for the respective settling velocities (w_{CaCO3}, w_{POC}), dissolution rate constant r_{CaCO3}, and the remineralization rate constant r_{POC}. The reaction losses in equation (6) for settling particulate material are balanced by appropriate source terms for dissolved species within the water column (i.e., for TAlk, DIC, phosphate, oxygen, and silicic acid). The new particle flux scheme allows individual specification of settling velocities for each particle species at each grid point as well as the choice of, for example, dissolution kinetics and solubilities depending on other three-dimensional variables such as in situ temperature. As a starting point, in the control run, values for w_{POC}, w_{CaCO3}, w_{opal}, r_{POC}, r_{CaCO3}, and r_{opal} are chosen which resemble closely the exponential e-folding-depth formulation as used by *Heinze et al.* [1999] and *Heinze and Maier-Reimer* [1999]. While r_{POC}, r_{CaCO3}, and r_{opal}

are set to 1.4 yr^{-1}, 0.5 yr^{-1}, and 0.1 yr^{-1}, the following expression is used for the settling velocity of opal:

$$w_{opal} = w_{basic} \cdot C_{w,opal}$$
$$C_{w,opal} = 1 \ (surface\ layer) \quad (7)$$
$$C_{w,opal} = 0.3 + 0.6 \cdot e^{-\alpha \cdot r_{opal}/w_{basic} \cdot Z} (deeper\ layers),$$

where w_{basic} is set to 3 m/d and Z (m) is the depth interval between the basis of the euphotic zone and the lower boundary of the respective model layer. Parameter α was set to a value of 0.3. The correction term $C_{w,opal}$ leads to gradual decrease of the settling velocity with depth, the correction being proportional to the dissolution rate constant r_{opal}. The choice for the particle flux parameters is associated with a large uncertainty. Particle settling velocities, dissolution rate constants, as well as remineralization rate constants are varying over a larger range in the ocean. If both parameters are multiplied with the same factor, the effect on the resulting particulate flux would not change even though each single parameter is completely wrong. We choose here 3 m d^{-1} as a mean settling velocity averaged over all particle size classes. This is consistent with estimates from observations [see e.g., *Kriest and Evans*, 1999] and a satisfying simulation of the marine ^{230}Th distribution [*Henderson et al.*, 1999]. The dissolution rate constant and α were adjusted to result in approximately the same combined particle attenuation functions as used by *Heinze et al.* [1999] in order to achieve correct dissolved water column concentrations of carbon cycle and nutrient tracers. The value of 0.1 yr^{-1} for the opal dissolution rate constant is in the correct range for untreated opal samples. The parameter choice at this stage was made in order to provide a reasonable first approximation for further refinements by a systematic optimization with respect to observations. As our model does not include a splitting of primary and secondary production, no difference is made in dissolution rates for diatoms (phytoplankton) and radiolarians (zooplankton). Such a differentiation would be possible in the seasonally resolving model version (HAMOCC3 [*Maier-Reimer*, 1993; *Six and Maier-Reimer*, 1996]; HAMOCC4 [*Hofmann et al.*, 2000]) which was not used here.

2.3. Porewater Chemistry and Porewater Diffusion

[11] Chemical porewater reactions and porewater diffusion are carried out simultaneously in an implicit numerical algorithm enabling time efficient integration of the model. The solid sediment components S (organic carbon, $CaCO_3$, opal, and clay) and dissolved components P (TAlk, DIC, phosphate, oxygen, and silicic acid) are coupled with each other by the reaction rate. Rather than computing directly the diffusion of the dissolved substance, here the diffusive transport of the respective undersaturations (or deviations from saturation concentration) simultaneously with the reduction of undersaturation due to chemical porewater reactions are determined,

$$\frac{dU}{dt} = \frac{\partial}{\partial z}\left(D_W \frac{\partial U}{\partial z}\right) - G, \quad (8)$$

where

U undersaturation (deviation from saturation concentration) (mol L^{-1});
G reaction rate (sink for undersaturation U from dissolution of solid material) (mol L^{-1} yr^{-1});
D_W diffusion coefficient for porewater diffusion (m^2 yr^{-1}).

As the reaction rate is proportional to the degree of undersaturation, this formulation can easily be used in an implicit numerical scheme regardless of the size of the time step and reaction kinetics without the risk of achieving negative tracer concentrations. The porewater diffusion coefficient D_W is set to 8×10^{-6} cm^2/s for all porewater tracers, which is in the range of the values given for individual tracer species by *Li and Gregory* [1974]. The change of a solid sediment component due to porewater reactions and particle deposition corresponding to equation (8) is (bioturbation is carried out in a separate step and is hence not stated in the following formula),

$$\frac{dS_*}{dt} = -G + Q, \quad (9)$$

where

S_* solid sediment component expressed in the same units as U (mol L^{-1});
G reaction rate (sink due to dissolution) (mol L^{-1} yr^{-1});
Q gain from particle rain (mol L^{-1} yr^{-1}).

The amount of matter subject to dissolution G per unit time depends on parameter r_c^*, the undersaturation U, and the amount of solid material available S_*,

$$G = r_c^* \cdot U \cdot S_*, \quad (10)$$

where for r_c^* we have

$$r_c^* = \frac{r_c}{P_{sat}}, \quad (11)$$

with

r_c reaction rate (yr^{-1});
P_{sat} saturation concentration in solution (mol L^{-1}).

For opal dissolution, a solubility P_{sat} of 800 μmol is used [cf. *Dixit et al.*, 2001]. For $CaCO_3$, the saturation concentration of carbonate is computed from the in situ solubility product after *Ingle* [1975] with pressure correction after *Edmond and Gieskes* [1970]. The reaction rate r_c computed from r_c^* = 40 L yr^{-1} mol^{-1} and P_{sat} = 800 μmol L^{-1} amounts to 0.032 yr^{-1} here, which is lower than the value used for the water column (0.1 yr^{-1}). It results from adjusting this parameter so that a satisfying reproduction of the water column silicic acid as well as sedimentary opal was achieved for the global Si throughput rate as given by *Tréguer et al.* [1995]. It reflects the need for accounting for alteration processes which slow down the reactivity of opal with aging of the sinking material. Variable dissolution rate constants and solubilities will be investigated in the model optimization further below. The ''undersaturation'' for organic carbon is given by the availability of oxygen (neglecting anaerobic respiration and associated effects of

Table 1. Si Data Sets for the Modern Ocean From the "SINOPS" Database Included Within the PANGAEA System[a]

Tracer Description	Unit	Number of Cycles
Opal sediment (on a calcite free basis), vertical average over bioturbated zone	weight-%	1854
$CaCO_3$ sediment, values at discrete depths	weight-%	18880
Opal sediment (relative to total sediment), values at discrete depths	weight-%	7571
$Si(OH)_4$ in the water column, full data set	μmol/L	352675
$Si(OH)_4$ in the water column, averaged data on model grid, all depths	μmol/L	15675
$Si(OH)_4$ in sediment pore waters	μmol/kg	6815
Opal flux through the water column, averaged, from long-term sediment trap deployments	mol Si/year	135

[a]These data were used for comparison with the model results.

denitrification and sulfate reduction). In discretized form, equation (9) becomes

$$\frac{S_*^{t+\Delta t} - S_*^t}{\Delta t} = -r_c^* \cdot U^{t+\Delta t} \cdot S_*^{t+\Delta t} + Q. \tag{12}$$

With the approximation

$$r_c^* \cdot U^{t+\Delta t} \approx r_c^* \cdot U^t, \tag{13}$$

the solid concentration $S_*^{t+\Delta t}$ is substituted in the G-term of equation (8) as a first approximation (that introduces formally a sizable deviation from the reaction rate constant, which originally has been chosen, only if the system is far away from equilibrium; this is not considered as critical):

$$S_{*\,first\ guess}^{t+\Delta t} = \frac{S_*^t + Q \cdot \Delta t}{1 + \Delta t \cdot r_c^* \cdot U^t}. \tag{14}$$

Schematically written, equation (8) is then solved numerically from

$$\frac{U^{t+\Delta t} - U^t}{\Delta t} = \frac{D_w^{upper}\left(U_{upper}^{t+\Delta t} - U^{t+\Delta t}\right) - D_w^{lower}\left(U^{t+\Delta t} - U_{lower}^{t+\Delta t}\right)}{2\Delta z^2} - \frac{r_c^* \cdot U^{t+\Delta t} \cdot \left(S_*^t + Q \cdot \Delta t\right)}{1 + \Delta t \cdot r_c^* \cdot U^t}. \tag{15}$$

Scheme (15) leads to a tridiagonal system of equations which can be readily solved by standard procedures. The final porewater concentrations and solid sediment concentrations after the diffusion-reaction step then become

$$P^{t+\Delta t} = P_{sat} - U^{t+\Delta t} \tag{16}$$

$$S_*^{t+\Delta t} = S_*^t - \Delta t \cdot r_c^* \cdot U^{t+\Delta t} \cdot \frac{S_*^t + Q \cdot \Delta t}{1 + \Delta t \cdot r_c^* \cdot U^{t+\Delta t}} + \Delta t \cdot Q. \tag{17}$$

The different chemical species are treated in the following sequence:

[12] 1. The clay fraction is added from particle rain (no reaction implemented so far).

[13] 2. Opal rain and dissolution plus silicic acid porewater diffusion are performed.

[14] 3. POC rain, remineralization, and porewater diffusion of oxygen and phosphate are carried out. The corresponding changes in DIC and TAlk are stored. The change in porewater CO_3^{2-} (carbonate ion) due to POC decay is computed.

[15] 4. $CaCO_3$ particle deposition and dissolution are computed where the degree of porewater saturation is approximated from the porewater values of TAlk and DIC at the old time levels plus the CO_3^{2-} reduction from POC remineralization.

[16] 5. Finally, porewater diffusion of DIC and TAlk is carried out (assuming constant porewater diffusion coefficients for all carbon species).

3. Database of Observations

[17] For comparison with the model results, a huge high quality database on oceanic Si cycle relevant observations was compiled. Since submitting data from the single scientist to the whole community is far away from being an automated procedure and no internationally binding regulation exists yet that secures the world's stock of valuable scientific data [*Dittert et al.*, 2001], a high-quality data collection on oceanic Si cycle relevant observations had to be built. Data were requested (1) from online accessible data centers (e.g.,World Data Centers); (2) by on demand access of scientific data centers (e.g., German Oceanographic Data Center); and (3) through CD-ROM distribution by scientific data management (e.g., British Oceanographic Data Center). However, personal data acquisition from the principal investigators (PIs) turned out to be the most promising approach to receive valuable data. Meta-information and analytical data were mapped on an n-dimensional catalogue in order to itemize the analytical value and to serve as unambiguous identifier [cf. *Dittert et al.*, 2002]. In practice, data management was carried out by means of the online-accessible information system Pan-European Network for Geological and Environmental Data (PANGAEA; http://www.pangaea.de/). Sharing data policy included that only published data were made available through the World Data Center for Marine Environmental Studies (WDC-MARE; http://www.pangaea.de/PangaVista?query=sinops), whereas unpublished and nonpublic data are kept under lock. Although some important data series were not yet for public use, most PIs agreed to exploit their data for evaluation of the model runs anyway. To protect the PIs, however, all data were anonymized. The Si tracer data sets as used for the model/observation comparison here are summarized in Table 1 and Figure 1.

4. Discussion of Control Run Results

[18] As a reference for subsequent sensitivity experiments on the marine silicon cycle and a first approximation for

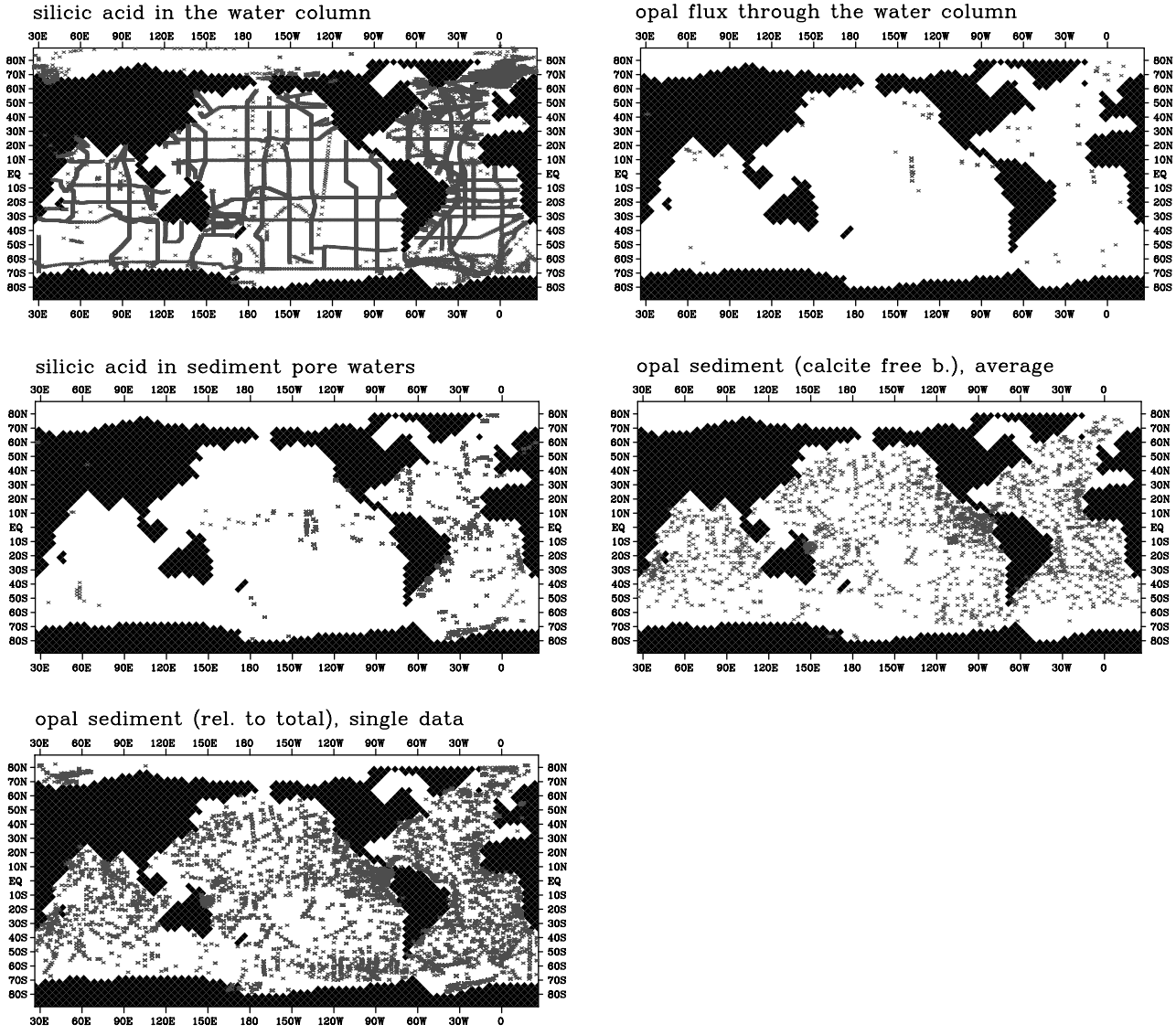

Figure 1. Data coverage of the marine Si database collated for and used in the comparison with the simulations (the database is available at http://www.pangaea.de/PangaVista?query=sinops).

further model optimization with respect to the observations, a control run was carried out. The model was integrated over 50,000 years. Important model parameters as used in this standard run are summarized in Table 2. Global bulk numbers as resulting for the reference run are listed in Table 3.

[19] The opal export production map (Figure 2a) reflects the gross pattern of the vertical velocity with high values in upwelling areas and low rates in the large oligotrophic midlatitudinal gyres. In spite of larger half saturation constants at low temperatures, the Southern Ocean opal export production is large here and of the same magnitude as in the equatorial Pacific Ocean. These high polar export production values support the study by *Pondaven et al.* [2000] that the high opal percentages in Southern Ocean sediments reflect in parallel to an elevated preservation efficiency high opal production rates, which have been underestimated previously. The resulting rain ratio of opal:POC (Figure 2b) and $CaCO_3$:opal (Figure 2c) in biogenic particle export production simulates the dominance of opal in upwelling areas and, in particular, the Southern Ocean. The Si/C ratios for opal:-POC (Figure 2b) are consistent with estimates from laboratory measurements [*Brzezinski*, 1985] as well as field observations, indicating high Si/C ratios in the Southern Ocean [*Nelson et al.*, 1995].

[20] The silicon tracers simulated were compared with the high-quality database as described in the previous section. Silicic acid concentrations in the water column (Figures 3 and 4) can be reproduced in their gross features by the model with low silicic acid values in the NADW (North Atlantic Deep Water) and continuously increasing concentrations along the global ocean conveyor belt. The contrast between NADW (Figure 3) and North Pacific intermediate to deep waters (Figure 4) is too low by about 30 μmol/kg. This is in agreement with the modeled natural radiocarbon

Table 2. Model Parameters as Set for the Control or Standard Run

Tunable Model Parameter	Value as Set for Control Run
Threshold value of particle export production ratio C(opal):C(POC) for the onset of $CaCO_3$ production [*Heinze et al.*, 1999, equation (5)]	0.7
Maximum possible production rain ratio $C(CaCO_3)$:C(POC) (see parameter r in equation (5) of *Heinze et al.* [1999])	0.3
Clay (dust) flux from continental weathering	1.0 g m^{-2} yr^{-1}
Global weathering input of Si	5.5×10^{12} mol Si yr^{-1}
Global weathering input of $CaCO_3$	15×10^{12} mol C yr^{-1}
Global weathering input of POC	4×10^{12} mol C yr^{-1}
$Si(OH)_4$ saturation concentration (“solubility”) in sediment pore waters	800 μmol yr^{-1}
Dissolution rate constant r_c^* for $CaCO_3$ sediment	1000 (yr^{-1} × mol)/L
Dissolution rate constant r_c^* for opal sediment	40 (yr^{-1} × mol)/L
Dissolution rate constant r_c^* for organic carbon sediment	50 (yr^{-1} × mol)/L
Degradation rate constant for dissolved organic carbon in the water column	0.05 yr^{-1}
Diffusion constant for pore waters D_w	8×10^{-6} cm^2/s
Coefficient for explicit bioturbation D_b	15 cm^2/1000yr

distribution [*Heinze*, 2002b] and hence a consequence of the velocity field applied here. Intermediate water $Si(OH)_4$ concentrations are significantly too high in the Pacific (Figure 4) and Indian Oceans (not shown). These can partially be explained by “nutrient trapping” in particles-only models (i.e., models which do not account explicitly for phytoplankton and zooplankton including their advection by the velocity field) such as the one used here [see *Najjar et al.*, 1992; *Aumont et al.*, 1999]. A solution to these discrepancies is the use of a more refined ecological model including zooplankton dynamics [see *Six and Maier-Reimer*, 1996]. A general problem is the too weak northward flux of Antarctic bottom water with relatively high $Si(OH)_4$ concentrations. This mismatch with the observations can at least in part be attributed to the vertical discretization and the low vertical resolution of the model in great depths.

[21] Opal sediment weight percentages on a calcite free basis (Figure 5) and relative to total sediment (Figure 6) as simulated in the control run show approximately the same qualitative picture as the observations: high concentrations under upwelling or deep water production areas such as in the equatorial regions, the Southern Ocean, and the north-

Table 3. Global Bulk Numbers as Resulting for the Model Control Run

Name of Variable	Value as Resulting for Control Run
Atmospheric pCO_2	277.7 ppmv
POC export production	8.66 GtC yr^{-1}
POC deposition onto sediment	0.12 GtC yr^{-1}
POC accumulation	0.048 GtC yr^{-1}
$CaCO_3$ export production	1.64 GtC yr^{-1}
$CaCO_3$ deposition onto sediment	0.42 GtC yr^{-1}
$CaCO_3$ accumulation	0.18 GtC yr^{-1}
Opal export production	185×10^{12} mol Si yr^{-1}
Opal deposition onto sediment	81.3×10^{12} mol Si yr^{-1}
Opal accumulation	5.5×10^{12} mol Si yr^{-1}
Dissolved organic carbon inventory (water column)	240.5 GtC
Organic carbon sediment pool	241.9 GtC
$CaCO_3$ carbon sediment pool	10096 GtC
Opal sediment pool	19986×10^{12} mol Si
Total dissolved inorganic carbon inventory	38778 GtC
Atmospheric carbon inventory	559 GtC

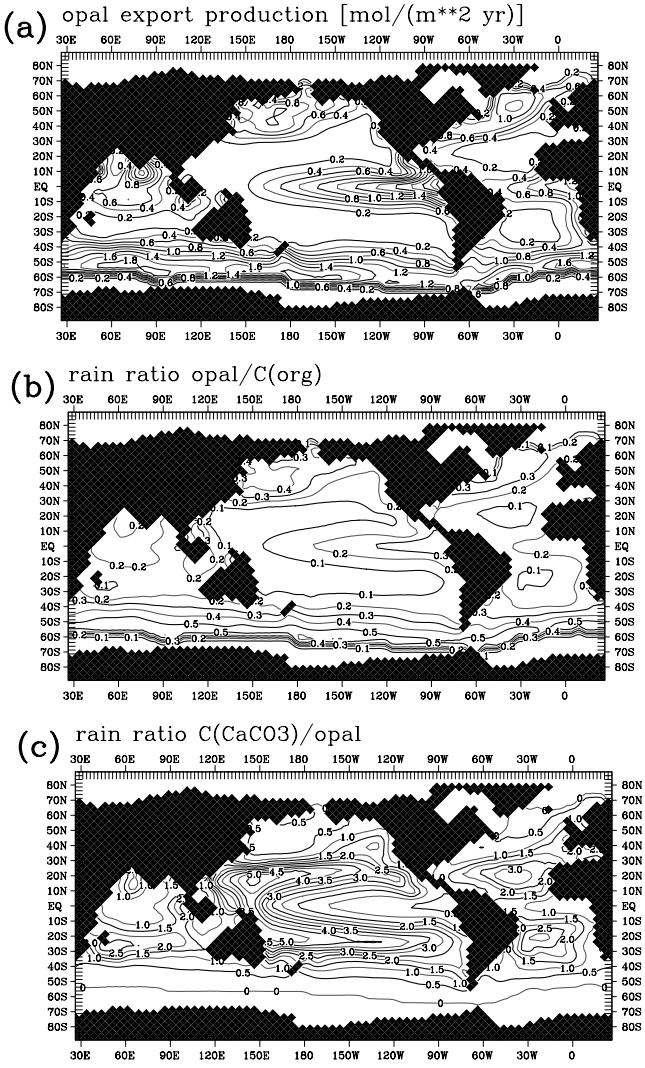

Figure 2. Results for the model control run. (a) Opal export production (in mol m^{-2} yr^{-1}). (b) Rain ratio opal:POC and (c) rain ratio $CaCO_3$:opal in the export production of biogenic particulate matter.

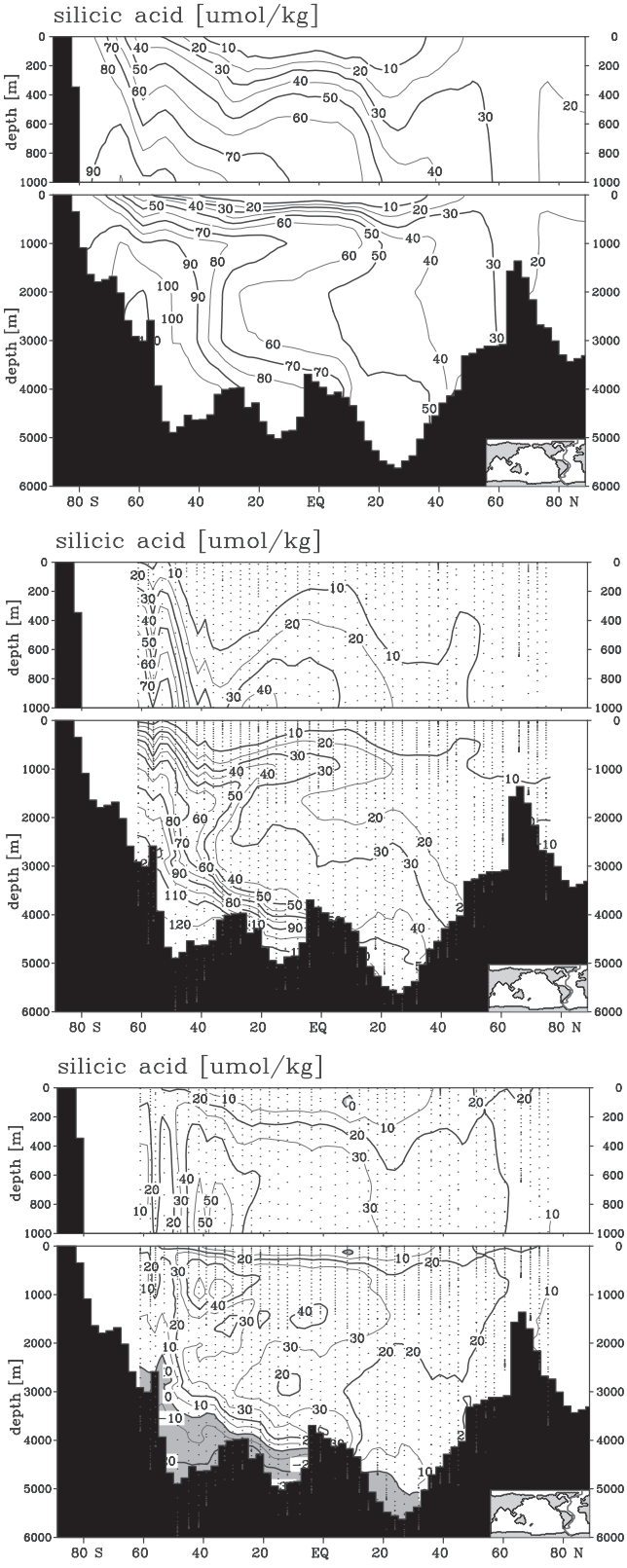

Figure 3. Silicic acid cross section along the western Atlantic. (top) Model (control run). (middle) Observations from the GEOSECS program [*Bainbridge*, 1981]. (bottom) Difference model – observations.

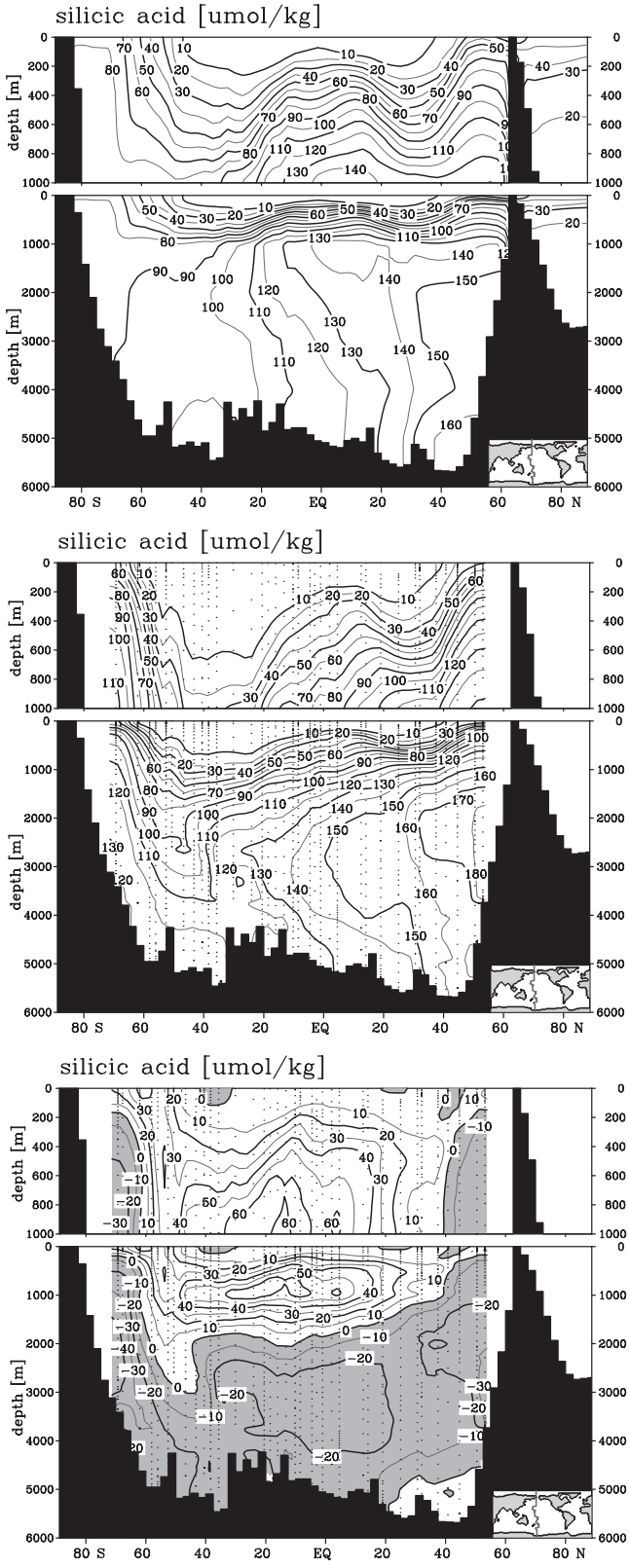

Figure 4. Silicic acid cross section along the western Pacific. (top) Model (control run). (middle) Observations from the GEOSECS program [*Craig et al.*, 1981]. (bottom) Difference model – observations.

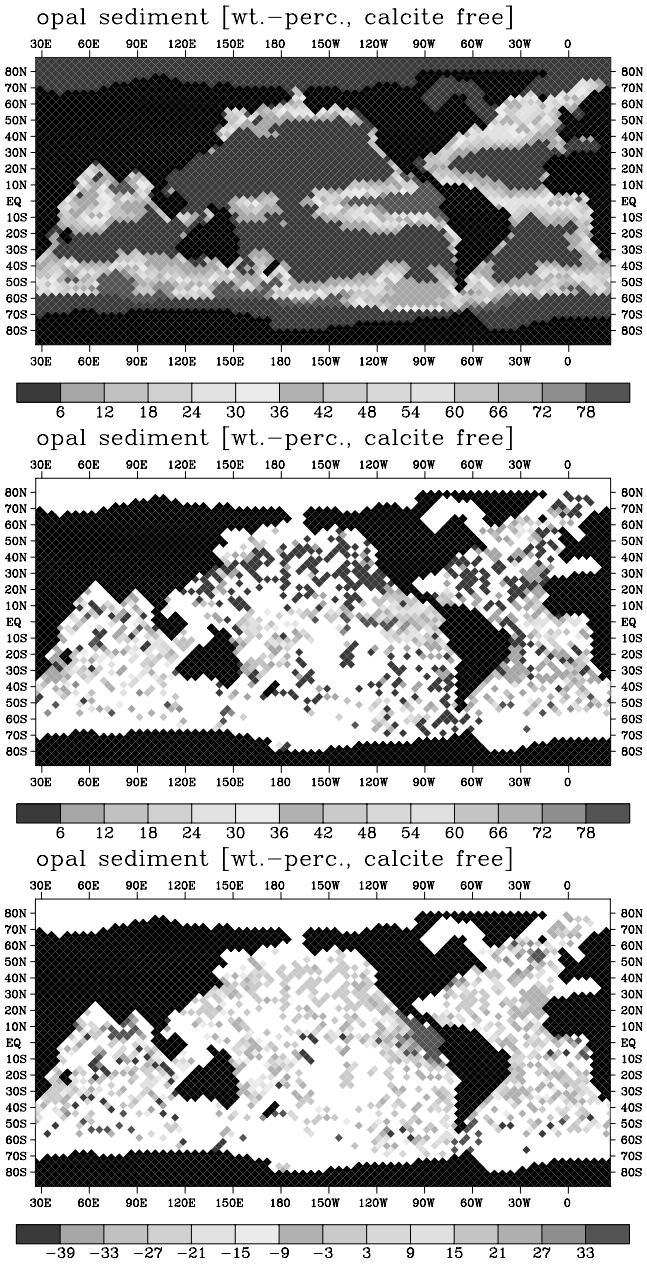

Figure 5. Opal sediment (weight-% on calcite free basis). (top) Model (control run). (middle) Observations (SINOPS data compilation http://www.pangaea.de/PangaVista?query=sinops). (bottom) Difference model – observations. (Comparison is based on averages over the entire bioturbated zone.) See color version of this figure at back of this issue.

west sides of both the Atlantic and Pacific. Modeled opal concentrations, however, are too high in the Gulf of Panama (eastern equatorial Pacific) as a consequence of nutrient trapping, and too low in the Indian Ocean. In the northwest Atlantic the opal sediment cover near the southeastern tip of Greenland is too pronounced when compared on a calcite-free basis and too weak when compared as relative to total sediment, possibly due to a general overestimation of export productivity in this model area. In the physical coarse resolution model providing the velocity field, deep water production tends to be too pronounced south of the narrow passages in the Greenland-Iceland-Scotland overflow areas and too weak north of them as compared with evidence from observations. Another explanation for the mismatch is mixing of biogenic sediment with inert material from

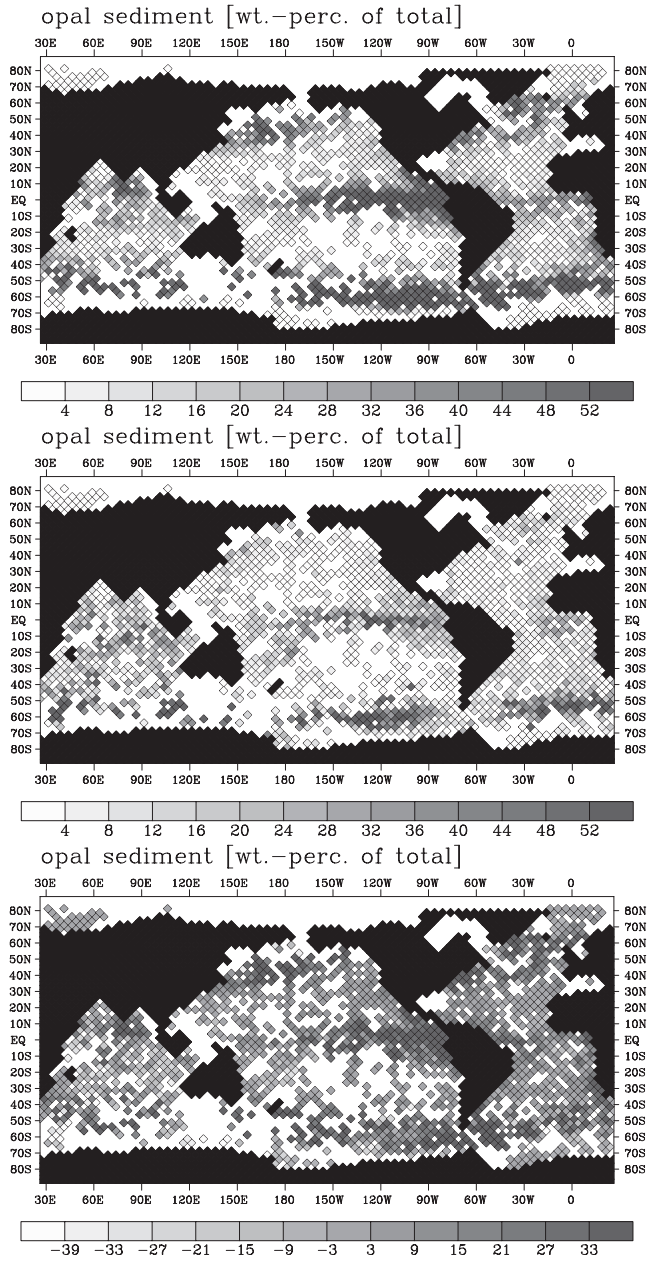

Figure 6. Comparison of model and data for opal sediment relative to total sediment weight (weight-% of total). Averages of all values within one grid cell were computed for this figure. (top) Model (control run). (middle) Observations (SINOPS data compilation http://www.pangaea.de/PangaVista?query=sinops). (bottom) Difference model – observations.

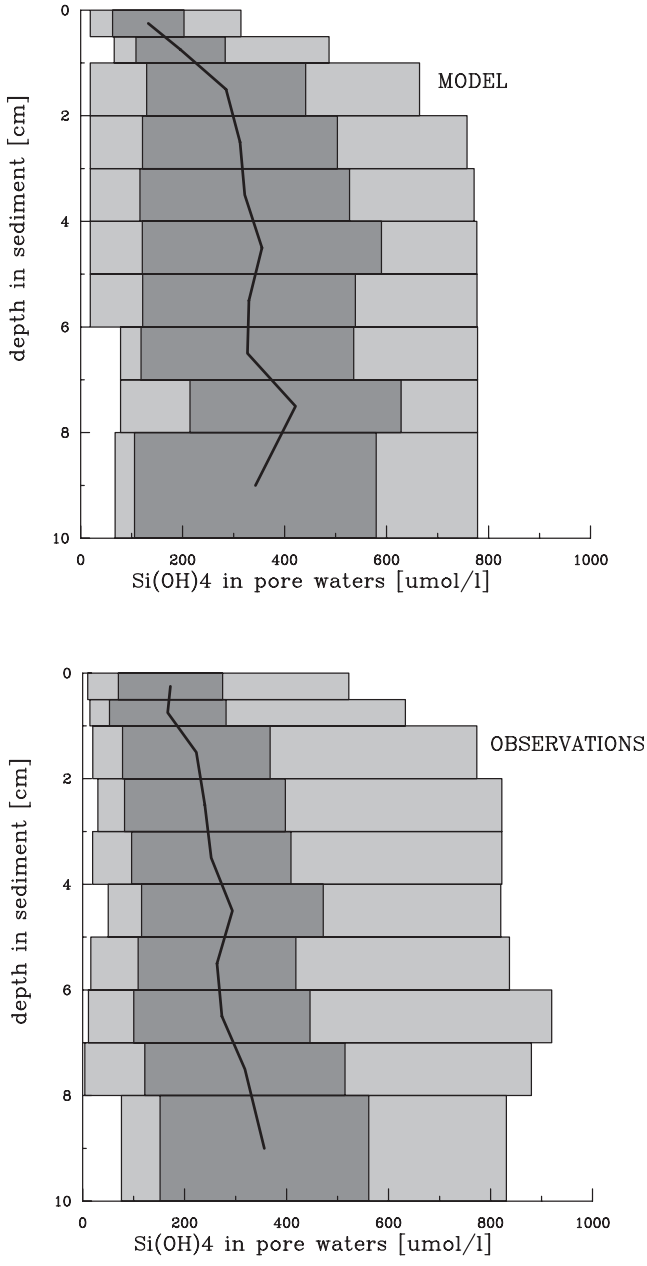

Figure 7. Mean porewater profiles of model and observations. Given are the mean (black line), the standard deviation (dark shading), and the extreme values (light shading) for each depth interval within the bioturbated sediment zone.

terrestrial origin (dust, ice rafted debris). The latter was applied here only as a constant aeolian flux all over the ocean. Local highs in clay material deposition are not yet included in the model.

[22] Porewater $Si(OH)_4$ profiles of the model in general are about 30% higher than corresponding measurements in sediment layers below the bottom water/sediment interface (Figure 7). On the average, the modeled values show a higher scatter around the mean value in a certain depth range. The range between maximum and minimum values agrees well between simulation and measurement below 3 cm within the sediment, while the model shows less variability in the upper 3 cm as compared to reality. The in general too high porewater silicic acid concentrations can be explained at least in part with the simplification of applying one value for opal solubility and dissolution rate in the control run. In reality, apparent opal solubilities vary between 1000 and 200 μmol/L due to a series of controlling factors such as reactive surface of siliceous shell material, contamination with aluminum, temperature, and organic coatings [e.g., *Van Cappellen and Qiu*, 1997; *Ragueneau et al.*, 2000]. Variable opal dissolution kinetics and solubilities will be addressed in the model sensitivity experiments further below.

[23] Opal fluxes through the water column in most cases are higher than corresponding measurements from sediment trap data (Figure 8). For our analysis, only data from long-term trap deployments (minimum 1 year) are used. A few trap data sets are added which have been deployed less than 1 year, but nevertheless, to the best knowledge of the originators, should be well representative for 1 year (corresponding integrated flux values where extrapolated to 1 entire year). Most sediment traps were placed in regions of large productivity gradients (Figure 1). Comparison of model results and traps at single locations can therefore easily result in large disagreements if, for example, ice cover or upwelling zones are slightly shifted between the real and the model worlds. No clear trend with strength of opal flux can be determined for the deviations of the modeled from the measured values. The relative error of the simulated opal fluxes (with respect to the observations)

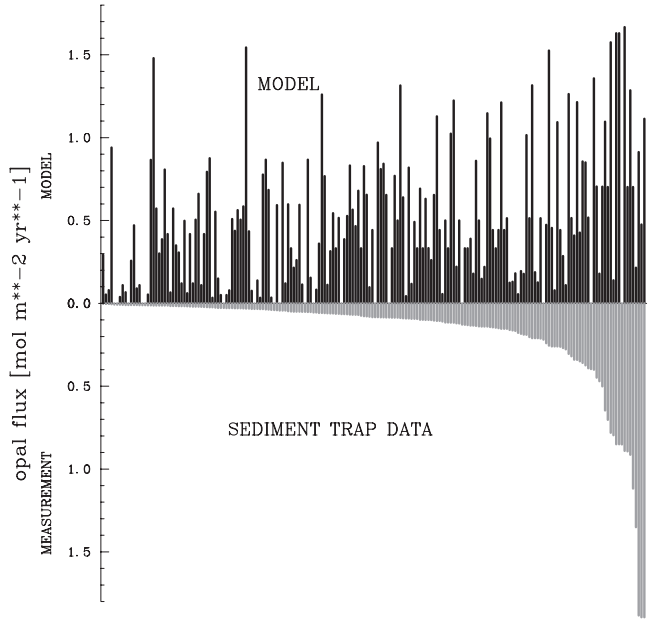

Figure 8. Overview on data of opal flux through the water column from long-term sediment trap deployments (light shading) and corresponding model equivalents (dark shading).

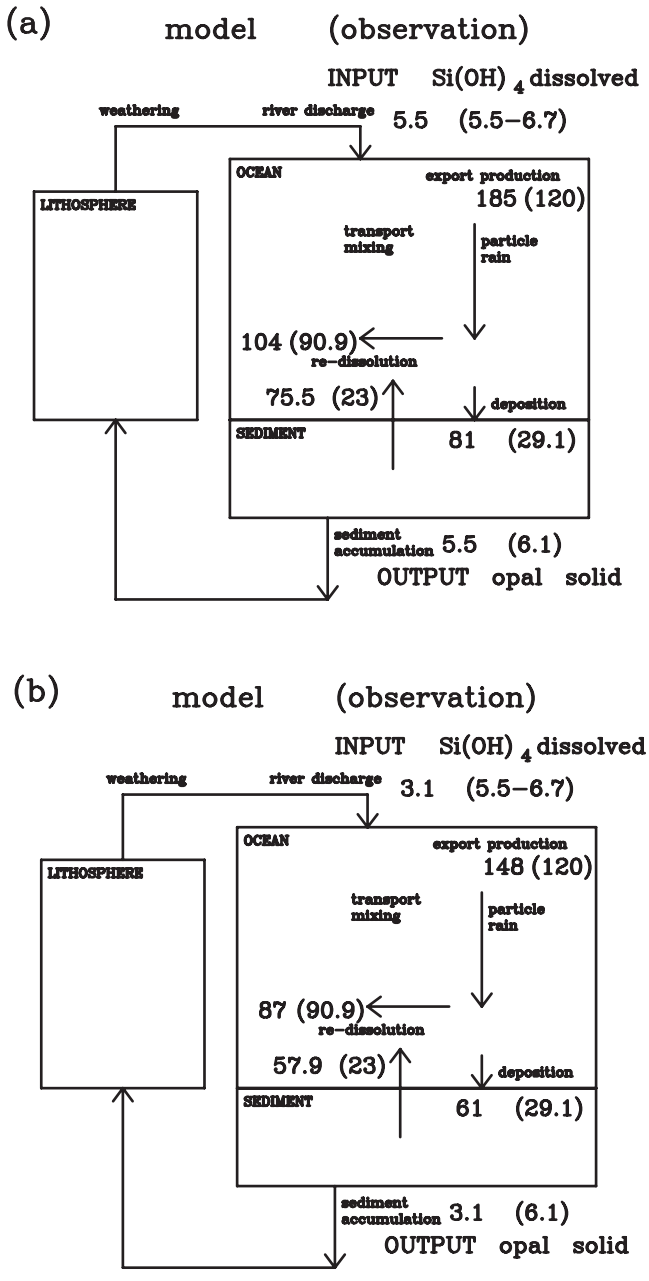

Figure 9. Comparison of the gross Si fluxes as resulting for (a) the control experiment and (b) the optimized model with estimates based on observations ([*Tréguer et al.*, 1995]: see values in parentheses). All fluxes are given in 10^{12} mol Si yr^{-1}.

increases at sites with low observed fluxes. These too high flux rates are surprising, in view of the reasonable values for the Si/C ratios in the surface ocean as well as the POC export production rate.

[24] The gross cycling of silicon for the control experiment can be compared with estimates of observations from *Tréguer et al.* [1995] (Figure 9a; Figure 9b shows for comparison the optimized Si cycle budget as described further below). The throughput rate of Si was chosen according to *Tréguer et al.* [1995] and therefore is a priori in agreement with the estimate from observations. The biggest mismatch between the control run and measurement concerns the dissolution pathway into the open water column $Si(OH)_4$. Compared to the observations, the export production of opal is about 50% higher in the model (185×10^{12} mol Si yr^{-1} compared to 120×10^{12} mol Si yr^{-1}). In view of the fact that also in the paper by *Tréguer et al.* [1995], the global export production rate was determined through a model (which was of the PANDORA box model type [see, e.g., *Broecker and Peng*, 1986] and hence considerably simpler than the one used here), the higher production rate in the simulation here could hardly be judged as better or worse than the 120×10^{12} mol Si yr^{-1} as given by *Tréguer et al.* [1995]. In fact, it was suggested by *Pondaven et al.* [2000] that the opal export production in the Southern Ocean might significantly exceed earlier estimates. While the dissolution of opal within the open water column agrees between model and data estimate, in the model, the deposition of opal to the sediment as well as the dissolution of opal from the sediment through porewater transport of $Si(OH)_4$ are overestimated. The difference between the simulated export production and the corresponding estimate from observations is of about the same magnitude as the difference in the sea floor opal dissolution rates.

[25] In the modeling study by *Gnanadesikan* [1999] a much lower global opal export production value of 89×10^{12} mol Si yr^{-1} (as compared to 185×10^{12} mol Si yr^{-1} in this study) was achieved for a combination of a temperature-dependent opal solubility in the water column and an eddy mixing scheme according to *Gent et al.* [1995]. As compared to our approach, the model used by *Gnanadesikan* [1999] differs considerably in the basic formulation of the biogeochemical Si cycling: (1) The opal production is forced by climatological sea surface $Si(OH)_4$ fields based on observations; that is, the model's surface silicic acid values are not predicted by the model. (2) The model is limited to the water column and does not include any sediment processes. Therefore this model circulates Si only within the water column and does not reproduce the unidirectional vertical transfer of several 10^{12} mol Si yr^{-1} from the ocean surface down to below the sediment mixed layer. This essential part of the Si cycle is missing in the model by *Gnanadesikan* [1999]. Hence no opal sediment distributions were provided for comparison with the real system. Together with a restoring to fixed surface $Si(OH)_4$, the global production rate of this model may thus be underestimated, even for a perfect velocity field.

[26] A further issue is the model's performance with respect to reproducing the natural ^{14}C. The velocity field applied in our study underestimates the age of water in the deep North Pacific [*Heinze*, 2002b]. The OGCM on which the study by *Gnanadesikan* [1999] is based has shown a tendency to severe radiocarbon age overestimation of deep waters in another publication [*Orr*, 2001]. From observations, *Broecker et al.* [1995] report a good correlation between silicic acid and natural $\Delta^{14}C$, which applies also for the HAMOCC model [*Heinze*, 2002b]. Potentially, calibration of the silicic acid in the water column to

observations in parallel to a too low $\Delta^{14}C$ in the water leads to an inconsistency in the work by *Gnanadesikan* [1999] between modeled $Si(OH)_4$ and $\Delta^{14}C$ values. If in the work by *Gnanadesikan* [1999], in fact, a too weak overturning would also occur, the resulting silicic acid values should be much higher in order to correspond to the too large radiocarbon ages and in order to follow the same linear trend of $\Delta^{14}C$ with respect to $Si(OH)_4$ as observed. This, of course, could bring back his opal export production rate values close to our estimate here.

[27] Inverse physical-biogeochemical simulations using the adjoint approach *Usbeck* [1999] result for an optimal reproduction of worldwide water column $Si(OH)_4$ data at a global opal export production value of about 200×10^{12} mol Si yr^{-1}, which is close to our value here. Likewise, the inverse model approach results in a general significant overestimation of opal particulate fluxes as compared to sediment trap data while retaining close to perfect temperature, salinity, and water column silicic acid distributions [*Usbeck*, 1999].

[28] Therefore the discrepancy between opal particle fluxes from sediment traps and modeling is not unique for our model and the possibility for a systematic error in the observations cannot be ruled out. Determination of sediment trap efficiencies using radionuclide calibrations has indicated that the trapping efficiency is in most cases lower than 100% (down to 15% in extreme cases) [*Yu et al.*, 2001; *Scholten et al.*, 2001; *Antia et al.*, 2001]. On the other hand, our comparatively simple model including only an annually averaged view may potentially lead to an overestimation of the vertical opal flux.

5. Introduction to the Optimization of the Model

[29] Though the model was able to reproduce prominent features of marine Si tracers, the results showed discrepancies between modeled tracer distributions and their observed counterparts. We now try to systematically improve the model on the basis of the Si data archive collated. We present a series of model sensitivity experiments in order to derive the response coefficients for a linear model which is solved for optimal model parameters. These coefficients describe how much one tracer changes at one location for a given change in a parameter which controls the Si cycle. Finally, the optimal Si cycle parameters are reintroduced into the full nonlinear three-dimensional HAMOCC model, and it is tested how much the modeled Si tracer distributions improved. The resulting gross marine Si budget will be discussed.

[30] The linear response model has the general form

$$\begin{aligned} \sum_{j=1}^{n} a_{1j}\Delta x_j &= \Delta g_1 \\ &.. \\ \sum_{j=1}^{n} a_{ij}\Delta x_j &= \Delta g_i \\ &.. \\ \sum_{j=1}^{n} a_{mj}\Delta x_j &= \Delta g_m, \end{aligned} \tag{18}$$

where Δx_j are the changes of the model parameters j to be applied so that the model renders tracer distributions as close as possible to the observations, Δg_i is the difference between the observed tracer i and the modeled analogue in the nonoptimized case (i.e., for the control run), and the a_{ij} are the linear response coefficients,

$$a_{ij} = \frac{\partial g_i}{\partial x_j}, \tag{19}$$

describing the change of a specific tracer value i at a specific point in three-dimensional space due to a change in parameter j. These response coefficients, here, were determined from sensitivity experiments with the full HAMOCC BOGCM relative to the unoptimized control run (please see the description of sensitivity experiments in the subsequent section). A total of $n = 15$ different sensitivity experiments was carried out. The problem was now to find the most appropriate way to adjust these 15 parameter changes in order to enable an optimal model simulation.

[31] The unknowns in equation (18), namely the parameter corrections Δx_j, were determined in the following way. The set of linear equations (18) is formally overdetermined. The least squares solution for the Δx_j is rendered by minimizing the cost function (matrices are indicated by markers on the left side of the letter representing the matrix for number of rows and on the right side of the letter for number of columns; the markers "$|$", "$_|$", and "$\cdot$" stand for "m", "n", and "1," respectively),

$$\begin{aligned} Q^2 &= \sum_{i=1}^{m}\left(\sum_{j=1}^{n} a_{ij}\Delta x_j - \Delta g_i\right)^2 \\ &= \left(\cdot\Delta x^T{}_{|}|A^T|_{|} - \cdot\Delta g^T|\right)\left(|A|_{|}\Delta x_{\cdot} - |\Delta g_{\cdot}\right), \end{aligned} \tag{20}$$

where

$$a_{ij} = \partial g_i/\partial x_j \Rightarrow \begin{pmatrix} a_{11}\ldots a_{1n} \\ \ldots\ldots \\ \ldots\ldots \\ \ldots\ldots \\ a_{m1}\ldots a_{mn} \end{pmatrix} = |A|$$

is the matrix of the response coefficients a_{ij} (see equation (19)) as determined from sensitivity experiments with the HAMOCC BOGCM. The minimal solution of the cost function (equation (20)) is found for $dQ^2/d(\Delta x) = 0$, i.e., for

$$|\Delta\hat{x}_j{}_{\cdot} = \left(|A^T|_{|}\,|A|\right)^{-1}|A^T|_{|}\,|\Delta g_{\cdot} \tag{21}$$

The minimum of the cost function was determined by application of the singular value decomposition (SVD) of coefficient matrix A. Details of this procedure are given by, for example, *Lanczos* [1961], *Wunsch* [1989], and *Press et al.* [1992].

6. Sensitivity Experiments

[32] The parameters and parameterizations as addressed in the sensitivity experiments cover a broad range of compart-

Table 4. Overview on Model Sensitivity Experiments and Associated Global Bulk Numbers for Biogenic Opal Export Production, Deposition Onto the Sediment, and Sediment Accumulation in 10^{12} mol Si yr^{-1}[a]

Experiment Number	Experiment Name	Export Production	Deposition	Accumulation
0	control run	184.8	81.3	5.5
1	K_s^{opal} scaled with dust input after *Andersen et al.* [1998]	191.1	83.2	5.5
2	K_s^{opal} scaled with dust input after *Mahowald et al.* [1999]	189.5	82.2	5.5
3	maximum K_s^{opal} value in cold regions doubled	186.4	81.6	5.5
4	V_{max}^{opal} doubled	152.8	68.1	5.5
5	V_{max}^{opal} reduced by factor 1/25 in equatorwards of 10° latitude	209.4	96.6	5.5
6	opal settling velocity reduced ($\alpha_{opal} \times 10$)	203.2	75.8	5.5
7	opal settling velocity dependent on opal export production	154.6	75.7	5.5
8	T dependent opal dissolution rate constant and solubility in water column	170.8	82.6	5.5
9	opal dissolution rate from sediment increased by factor 3.5	276.6	107.1	5.5
10	T dependent opal solubility in sediment	190.6	84.3	5.5
11	opal solubility in sediment dependent on opal rain rate	184.7	81.3	5.5
12	opal solubility in sediment dependent on detritus:biogenic opal	184.7	81.3	5.5
13	opal solubility and dissolution rate constant in sediment dependent on depth in sediment	155.6	67.8	5.5
14	clay input × 4	178.8	79.1	5.5
15	Si weathering × 1.5	207.4	95.8	8.7

[a] K_s^{opal} = half saturation constant for opal production, V_{max}^{opal} = maximum uptake rate of silicate, and α_{opal} = parameter steering the decrease of the settling velocity of opal particles with depth (see equation (7)).

ments and processes of the marine Si cycle (Table 4). Experiments 1–5 deal with a modification of nutrient uptake kinetics in the surface ocean and hence opal production. In experiments 6–8, changes in the parameterizations of the $BSiO_2$ particle flux in the water column are investigated. Parameterizations of opal dissolution from the sediment are addressed in experiments 9–13. Finally, two studies were carried out concerning the linkage of the marine Si distributions to continental sources (experiments 14–15).

[33] In the surface ocean experiments, the two parameters maximum uptake velocity V_{max}^{opal} (see equation (2)) describing the maximum nutrient uptake rate (plankton growth), and the half saturation constant K_s^{opal} (see equation (2)) describing the slowing down of nutrient uptake at lower nutrient levels were changed with respect to the model control run. For experiments 1 and 2, K_s^{opal} was rescaled with two different modeled fields for atmospheric dust deposition onto the sea surface (from the atmospheric model simulations of *Andersen et al.* [1998] and *Mahowald et al.* [1999]). These experiments take into account the fertilizing or biolimiting effect of iron which is one component of continent derived atmospheric dust loads. The exact mechanisms for enhancing phytoplankton productivity through Fe addition is not yet identified [e.g., *Geider and LaRoche*, 1994]. The scaling of K_s^{opal} was carried out as follows: First, a maximum possible value for K_s^{opal} was defined, namely 20 μmol/L corresponding to no iron addition from the atmosphere. K_s^{opal} then was lowered by adding the dust deposition (measured in mg m^{-2} d^{-1}) using 0.1 μmol/L as a lower cutoff value at very high dust depositions. The corresponding two-dimensional distribution for K_s^{opal} was then normalized to the corresponding area integral of K_s^{opal} for the control run. In order to see a somewhat larger response of the model, finally, the K_s^{opal} values were multiplied by a factor of 3 (Figure 10). In a further experiment on K_s^{opal} (experiment 3), a doubling of the half saturation constant for Si uptake in cold regions was tested (Figure 10). This change leads to correspondingly elevated surface $Si(OH)_4$ values in polar regions and hence increased preformed $Si(OH)_4$ concentrations. In contrast to this effect, a change in the uptake velocity parameterizations lead primarily to a change in the horizontal gradients for the opal export production, which became clearly higher for a doubling of V_{max}^{opal} (experiment 4). Additionally, a strong reduction of V_{max}^{opal} (by a factor of 1/25) within an equatorial band between 10°N and 10°S was investigated (experiment 5). This modification leads to a strong reduction of opal production in the eastern equatorial Pacific and hence to a suppression of the effect of ''nutrient trapping'' in particles-only models such as the one used here [*Najjar et al.*, 1992; *Aumont et al.*, 1999].

[34] For particle flux through the water column, the first two experiments addressed the settling velocity of opal particles. In a first experiment the slowing down of the settling velocity with depth was modified by increasing factor α (see equation (7)) by 10, leading to a stronger slowing down of settling velocity with depth (which has the same effect as an increase of the dissolution rate) (experiment 6). In a second study, the settling velocity was made dependent on the opal export production rate, assuming that larger particles form in high production zones and settle faster according to less effective Stokes friction (experiment 7). The original settling velocities were multiplied by the opal production rate (in mol Si cm^{-2} yr^{-1}). Afterward, the complete volume integral of settling velocities was normalized to the corresponding integral of the reference run. In the last water column experiment, temperature-dependent opal dissolution rate constants and solubilities were considered (experiment 8). For the solubilities, the functional relationship of *Van Cappellen and Qiu* [1997] was applied. For the dissolution rate constants, several representations of the literature were investigated. Finally, a new formulation was derived. For the derivation of the temperature-dependent water column dissolution rate constants as well as the depth-dependent dissolution rates of opal within the sediments, mostly experimental data of *Rickert* [2000] were used. In Figure 11 (top), untreated single opal samples from the

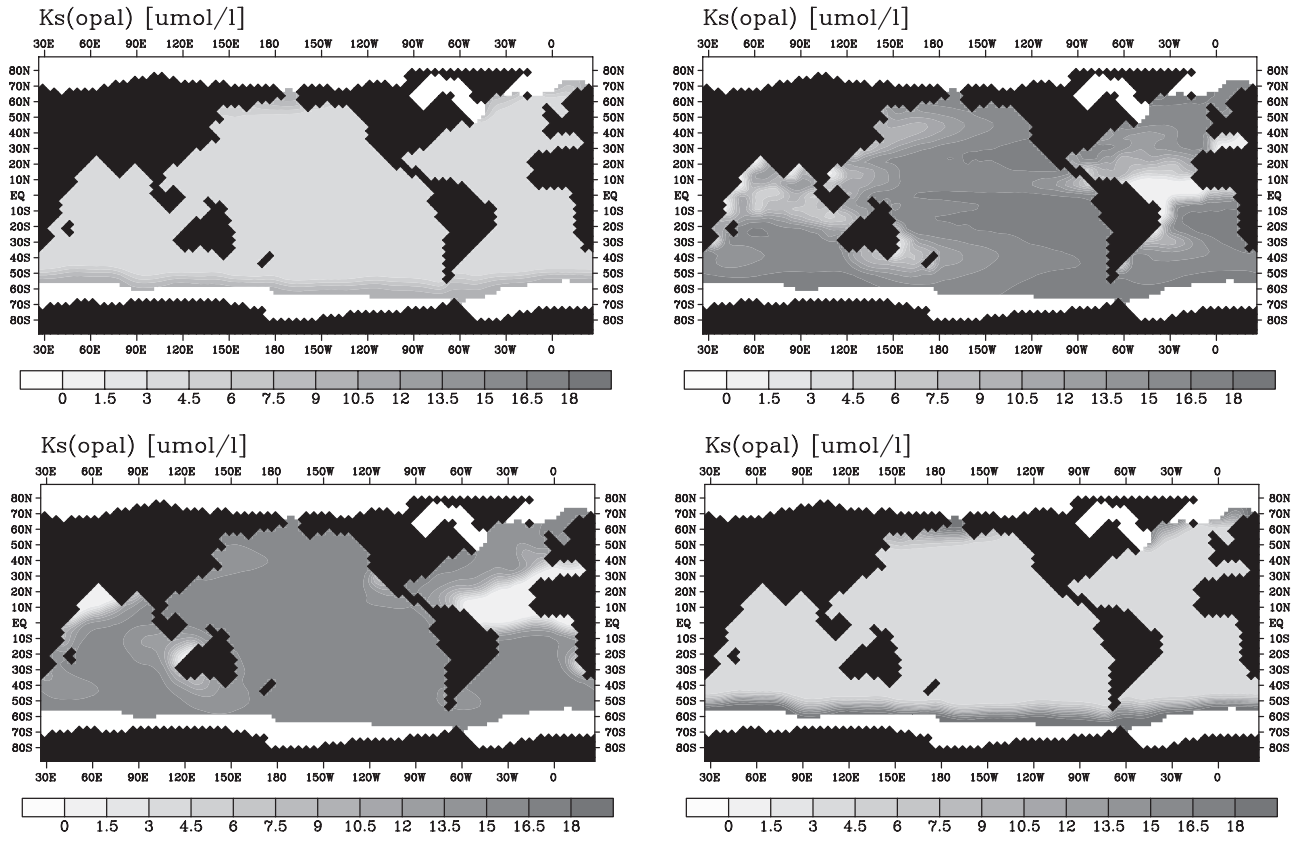

Figure 10. Half saturation constants for opal uptake. (top) Left: control run; right: scaled by dust input after *Andersen et al.* [1998]. (bottom) Left: scaled by dust input after *Mahowald et al.* [1999]; right: for increase of dust input in cold regions.

water column and the sediments of the Norwegian Sea, the North Atlantic, and the Weddell Sea are illustrated. In order to assess the temperature effect on the opal dissolution, the apparent dissolution rate constants (μmol g^{-1} h^{-1}) of each sample from continuous flow-through (CFT) experiments determined at 2°C were converted to a temperature range of 0–30°C using the equation

$$\ln k_1 = \ln k_2 + \frac{E_a}{R}\left(\frac{1}{T_1} - \frac{1}{T_2}\right), \tag{22}$$

with

k_1 rate constant for CFT dissolution reaction at temperature T_1 (°K);
k_2 rate constant for CFT dissolution reaction at temperature T_2 (°K);
E_a average activation energy of 60 kJ mol^{-1};
R universal gas constant (8.314 J K^{-1} mol^{-1}).

The CFT dissolution rate constants, however, do not correspond to the specific dissolution rate constants (V_{dis}), which serve as a measure of opal dissolution in natural environments and are common in the literature. The values were converted to V_{dis} by means of the specific surface area and the mass of $BSiO_2$ of the sample involved in the experiment as well as the particular apparent solubility (Si_{eq}). The latter is also temperature dependent and was calculated for the temperature range of 0–30°C following the equation of *Van Cappellen and Qiu* [1997],

$$\log Si_{eq} = 6.44 - \frac{968}{T}. \tag{23}$$

The resulting V_{dis} values for temperatures between 0° and 30°C (Figure 11, top) vary by a factor of up to 20 mainly due to large differences in specific surface areas of the samples. The samples with largest surface areas reveal highest rate constants. To eliminate the effect of specific surface areas, the dissolution rate constants were normalized to an average value of 30 m^2 g^{-1} (Figure 11, bottom). A mean fit was estimated and introduced in the model,

$$V_{dis} = 2.06 \cdot 10^{-5}\, T^3 - 5.09 \cdot 10^{-5}\, T^2 + 7.83 \cdot 10^{-3}\, T + 5.61 \cdot 10^{-2}. \tag{24}$$

For comparison, values of previous studies are included in Figure 11.

[35] Five different experiments were carried out about opal dissolution in the bioturbated sediment zone. In experiment 9 the rate constant for opal dissolution from the sediment was increased by a factor 3.5. In the next experiment the temperature dependency of the opal solubility after

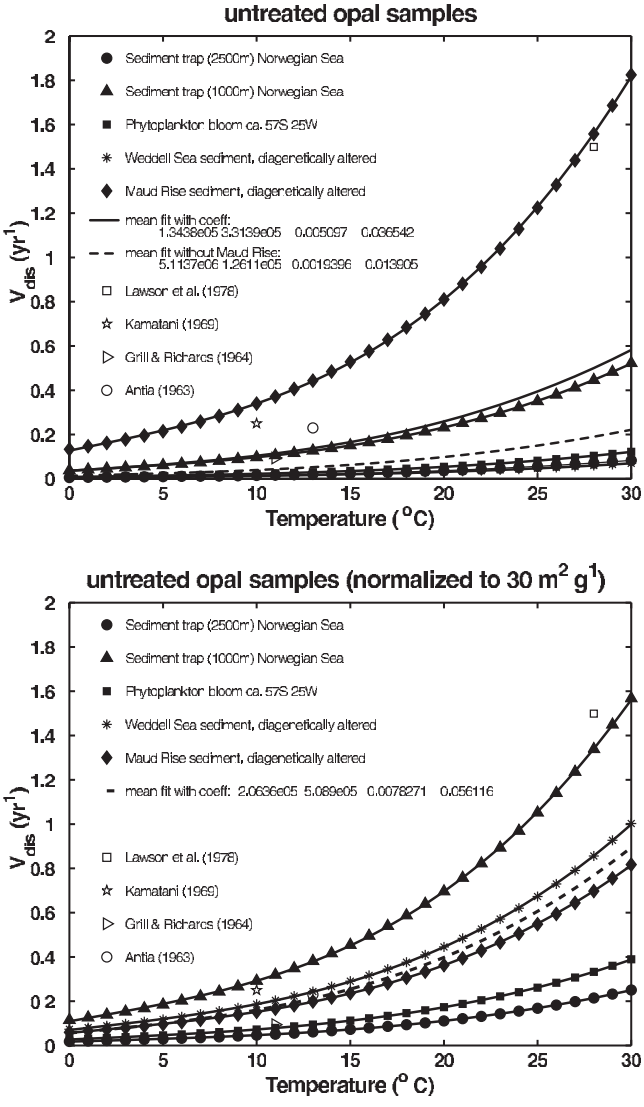

Figure 11. Dissolution rate constants V_{dis} of untreated opal samples in the water column (top) in dependence of temperature and (bottom) normalized to mean specific surface area of 30 m^2 g^{-1}.

Van Cappellen and Qiu [1997] (see equation (23)) was tested separately instead of using a constant porewater $Si(OH)_4$ saturation concentration of 800 μmol/L (experiment 10). Besides the temperature dependency, dissolution of opal from the sediments can be influenced by differential reactivity of the opaline material or by mixture with clay particles and modification of biogenic opal into less soluble aluminosilicates. In order to test potentially promising parameterizations of these processes, three experiments were carried out on the basis of flow through experiments. The first opal solubility parameterization is based on a dependency on the opal rain rate (Figure 12),

$$S_{opal} = 164.7 \cdot ln(opal_{rain}) + 927.28, \qquad (25)$$

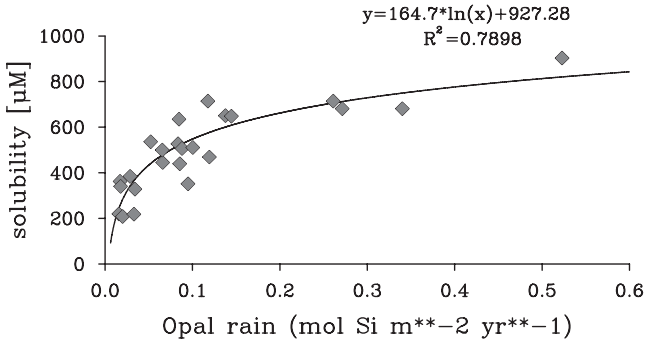

Figure 12. Opal solubility in the bioturbated sediment zone according to flow-through experiments as a function of the opal rain rate (based on rain rates as derived by *Ragueneau et al.* [2000]; solubility data from *Dixit et al.* [2001], *Gallinari et al.* [2002], and *Rickert* [2000]; sediment measurements from *Van Bennekom et al.* [1988], *DeMaster et al.* [1992], *Dymond and Lyle* [1994], *McManus et al.* [1995], *DeMaster et al.* [1996a, 1996b], *Sayles et al.* [1996], *Schneider et al.* [1996], *Berelson et al.* [1997], *Koning et al.* [1997], *Rabouille et al.* [1997], *Ragueneau et al.* [2001], and O. Ragueneau, unpublished data, 1999).

where S_{opal} is the opal solubility in μmol/L and $opal_{rain}$ is the opal flux rate through the water column in mol Si m^{-2} yr^{-1} (experiment 11). The second solubility parameterization represents a dependency on the ratio of detrital (inert) to biogenic material within matter which was deposited onto the ocean floor (Figure 13) (experiment 12),

$$S_{opal} = -102.26 \cdot ln(ratio_{det:bio}) + 699.05. \qquad (26)$$

Both parameterizations were derived from measurements by *Dixit et al.* [2001], *Gallinari et al.* [2002], and *Rickert* [2000]. A dependency of the solubility on the rain rate might be possible due to changes in biomineralization at different growth rates. A rain rate dependent solubility

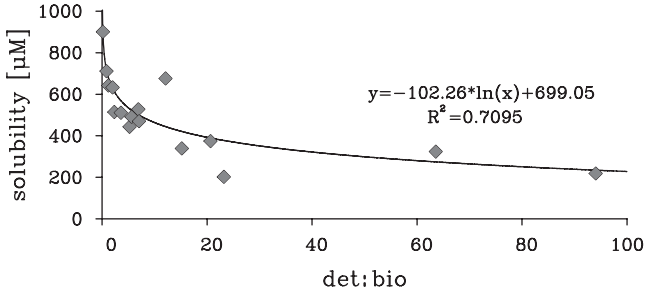

Figure 13. Opal solubility in the bioturbated sediment zone according to flow through experiments as function of the ratio of detrital material to biogenic opal (based on solubility data from *Dixit et al.* [2001], *Gallinari et al.* [2002], and *Rickert* [2000]; use of sediment measurements from *Dymond and Lyle* [1994], *Honjo et al.*, 1995; *McManus et al.*, 1995; *Rabouille et al.*, 1997; *Van Cappellen and Qiu*, 1997; *Ragueneau et al.*, 2001; and O. Ragueneau, unpublished data, 1999).

could be successfully used by *Archer et al.* [1993] to explain regional differences in opal sediment content. The changes in solubility in the presence of clay material can occur due to a partial conversion of biogenic opal into clay minerals when dissolved aluminum (from the clay minerals) is available. This conversion of process of originally biogenic material into clay minerals is also termed "reverse weathering" [e.g., *Michalopoulos and Aller*, 1995].

[36] Furthermore, a depth-dependent formulation of the dissolution rate constant (dissolution kinetics) was derived on the basis of data from flow through experiments and tested in experiment 13. In order to describe realistic terms of opal dissolution in the Sediments, an analytical approach using the 1-D diagenetic equation according to *Berner* [1980] has been chosen, ignoring dynamics (i.e., advection and mixing of solid and liquid phases due to bioturbation) and assuming steady-state conditions. Hereby the observed silicic acid, porosities, and biogenic silica profiles of 13 locations with different depositional environments, and hence different opal/detritus ratios were selected as depth-dependent parameters to calculate reactivity constants (k_B) and silicic acid fluxes through the sediment-water interface. In this inverse modeling approach the observed data were fitted with exponential functions, except for $BSiO_2$ contents where also linear decrease functions were used. Figure 14 shows the evaluated depth-dependent dissolution rate constants from different oceanic regions. The maximum and minimum k_B values in the Weddell Sea and the North Atlantic diverge approximately by 2 orders of magnitude. A mean fit of

$$k_B = 3.09 \cdot 10^{-2} + (0.13 - 0.03) \cdot e^{-1.21 \cdot \text{depth}} \qquad (27)$$

was formulated (unit for k_B: [yr^{-1}]). The relationship was introduced into the model through shifting it so that the k_B value one resulting from the mean fit coincided with the original value from the control run for the sediment water interface.

[37] Finally, two simple experiments were carried out in which the continentally derived input of matter to the ocean was modified. The atmospheric clay flux was increased by a factor of 4 in order to test the effect of a higher dilution of sedimented matter with refractory materials (experiment 14). A modest increase of the Si weathering flux into the ocean by 60% was investigated in a last experiment (experiment 15).

[38] All sensitivity experiments were initialized by homogeneous tracer concentrations in the water column and the sediment porewaters and inert clay only sediment. Each run was integrated into quasi-equilibrium over 100,000 years. The resulting values for opal export production and deposition of matter onto the sediment are summarized in Table 4.

7. Optimization Procedure

[39] We chose $Si(OH)_4$ in the water column, $Si(OH)_4$ in sediment porewaters, opal sediment on a calcite-free basis (vertical average over the bioturbated zone), and opal sediment relative to total sediment (measurements from discrete depths) as relevant tracer records for the fitting procedure (see Table 1). Opal flux data from sediment trap records were

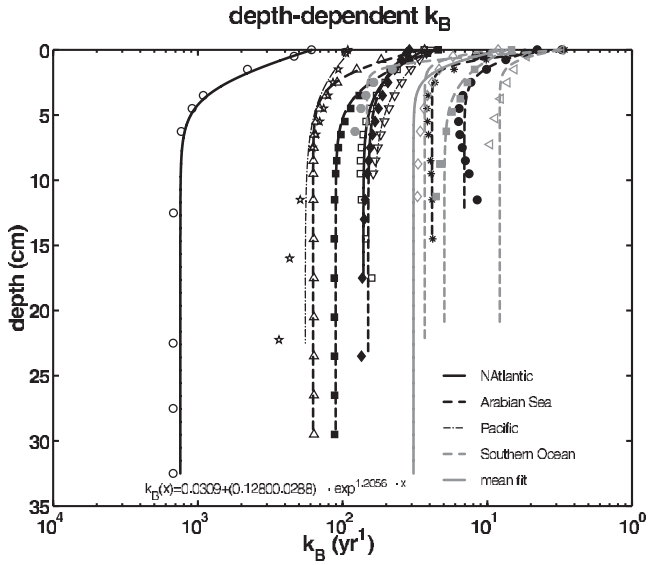

Figure 14. Exponentially fitted depth-dependent reaction rate constants (k_B).

not used for the optimization due to potential systematic errors associated with them. The $Si(OH)_4$ data set for the water column was split into two separate files, one for shallow samples down to 1000 m, and one for deep values below 1000 m, in order to weight corresponding measurements differently. At first, the tracers were normalized by weighting them with a characteristic perturbation value in order to avoid a preferential fit to one or more tracers due to differences in physical units and variance of oceanic distributions. A normalization with respect to number of tracer data per tracer type was not carried out, so that tracer species corroborated by a larger number of data were preferentially used for optimization. All parameter changes as tested directly in the sensitivity experiments were associated with the length 1. Therefore resulting values for the optimal parameters close to 0 would indicate a value close to the reference run counterpart, optimal parameters near 1 would indicate that the parameter as in the sensitivity experiment would be close to the optimal one. Likewise, for the sensitivity experiments, where full parameterizations were exchanged, an optimal parameter near 1 indicates "on" for the new parameterization (and "off" for the control run formulation) and vice versa.

[40] At first, a fit of all 15 model parameters as tested before in the sensitivity experiments was attempted. The system of equations (18), however, proved to be in fact underdetermined (though it appears formally to be overdetermined). According to the SVD and the associated trade-off between length of the solution vector for the parameters and goodness of fit, a potential maximum of about seven parameters could be determined independently from the system.

[41] In order to make a more appropriate choice for the parameter changes to be the most promising ones, every single parameter was estimated separately from the others by fitting the response model to the data and by analyzing

Table 5. Optimized Values for Combined Estimates of Model Parameters, Retaining Only the Five Parameters With the Largest Improvement[a]

Experiment Name	Optimal Parameter
V_{max}^{opal} doubled	−0.36
Opal settling velocity dependent on opal export production	0.26
Opal solubility and dissolution rate constant in sediment dependent on depth in sediment	0.68
Clay input times 4	0.76
Si weathering times 1.6	−1.17

[a]A parameter change 1 corresponds to full switch of a parameter change as tested in the sensitivity test. Values smaller than 0 indicate a parameter change in the opposite direction.

the anticipated improvement in goodness of fit. Not taking into account the parameters that yielded unrealistic directions of change for best fit to the observations, the five parameters with the largest ''improvement potential'' were the depth-dependent opal dissolution kinetics, the productivity-dependent opal settling velocity, the general change in maximum Si uptake velocity V_{max}^{opal}, and the clay as well as the Si input from continental weathering.

[42] These five parameters were retained in the following analysis while the others were ignored. By applying the SVD technique, again their optimal value was determined, simultaneously this time. As it turned out that the improvement in the reproduction of certain tracer types was sometimes achieved for a dramatic deterioration in goodness of fit for deep $Si(OH)_4$ values in the water column, the deep water $Si(OH)_4$ concentrations were weighted twentyfold in order to keep the modeled tracers closer to the observations at great depths. Realistic values for all parameters were now achieved for a maximum number of three independent parameters. The result is shown in Table 5. The associated new parameters for input of matter are a clay input of 3.3 g m^{-2} yr^{-1} and an Si input of 3.1×10^{12} mol Si yr^{-1} (instead of respective values 1 g m^{-2} yr^{-1} and 5.5×10^{12} mol Si yr^{-1} in the control run). The corresponding parameter adjustments were reintroduced into the full nonlinear three-dimensional HAMOCC BOGCM. A complete run restarting from homogeneous tracer concentrations in porewaters and water column as well as clay only sediment was carried out.

8. Discussion of the Model Optimization

[43] We now discuss first the change in the model's goodness of fit to the observations and then return to the marine Si budget quantification. For the three-dimensional model, the overall change in goodness of fit was somewhat smaller than the change as anticipated from the linear model. However, the improvement was significant (Table 6). At first sight, the overall minor improvement in goodness of fit (altogether the rms error of the modelled Si tracers with respect to observations could be reduced by only 7%) may seem disappointing. Potentially, the goodness of fit can be improved further. The modest improvement of the fit may be due to limitations in both parts of the model, the biogeochemical as well as the physical part.

[44] The standard model run may have been already close to the optimal solution within the given model configuration. The biogeochemical module is based on a series of empirical formulations such as the Michaelis-Menten nutrient uptake kinetics and dissolution rates based on laboratory experiments and associated curve fitting. Also, it should be kept in mind that it averages over the annual cycle and thus may underestimate vertical particulate fluxes. The model does include only very crudely three ''functional groups'' (opal shell producers, $CaCO_3$ shell producers, and organisms building no shell material) and does not differentiate between different sizes classes as well as primary, secondary, and tertiary biological production. Further, processes essential to the marine Si cycle may still have to be identified and introduced into the model.

[45] The simulated distributions cannot match the observed values as long as the model velocities do not exactly coincide with those of the real world. An overestimated upwelling may govern the results due to nutrient trapping. Locally, this shortcoming can lead to an overestimation of the opal export flux as well as the opal sediment percentage (especially in the eastern equatorial Pacific). A strong reduction of the opal export production in this area (see sensitivity experiment 5), however, did not lead to a plausible solution for this problem. A slight shift of upwelling zones between model and real world can further lead to discrepancies between model and observations which cannot be remedied by changing only the biogeochemical parameterizations. The general tendency of the optimized solution for too low deep water silicic acid deep water concentrations, clearly, reflects the too weak gradients in deep water age in this coarse resolution model. It is expected that a significant part of this deficiency could be removed by a better vertical model resolution. A respective 22-layer model shows a remarkably improved $\Delta^{14}C$ (of DIC) simulation. As natural radiocarbon and silicic acid are fairly well correlated in sea water [*Broecker et al.*, 1995], a corresponding improvement of the silicic acid simulation in the water column can be expected. A better rendition of the deep water production processes including the overflows across the Greenland-Scotland ridge system will further contribute to steepen the gradients of model water column

Table 6. Change in Goodness of Fit for Best Simultaneous Estimate of the Five Parameters With Largest Improvement Potential for the Linear Response Model and for the Full Nonlinear Three-Dimensional Model[a]

Experiment Name	Opal Calcium-Free Basis	Opal Relative to Total	$Si(OH)_4$ Water Column (<1 km)	$Si(OH)_4$ Water Column (>1 km)	$Si(OH)_4$ Sed. Porewater	All
Linear model	5.85	14.70	25.07	−7.34	11.37	11.64
Three-dimensional model	2.15	4.21	6.20	0.01	16.79	6.97

[a]Units for opal values are weight percent, for $Si(OH)_4$ μmol/L, and for all tracers together normalized units.

tracer concentrations. We consider here a self-consistent model system which is open only for input of matter from the continents and output by sediment accumulation; we expect, however, that the biogeochemical parameters cannot be adjusted arbitrarily in order to override weaknesses in the flow field simulation. As sediment and water column interact with each other, resulting errors of parameters and tracer distributions for the water column cannot be "hidden" in the sediment and vice versa. Specifically, this is reflected in the limitations of the improvement in goodness of fit. This result coincides with a study on anthropogenic tracers, where adjustments of the tracer delivery functions could not override weaknesses in the ocean model velocity field [*Heinze et al.*, 1998].

[46] Besides the changes in goodness of fit for the runs using the optimized parameters, these show significant changes in tracer distributions as compared to the control run. For water column $Si(OH)_4$, the basic tracer structures are retained in the optimized run while concentrations are generally somewhat lower. This leads to a better reproduction of the upper ocean silicic acid concentration as well as to improvements of the deeper Atlantic and the eastern equatorial Pacific Ocean, while for the deep northern Pacific, too low values are achieved. Overall, the opal sediment reproduction could be significantly improved for both presentation methods, on a calcite-free basis (Figure 15) and relative to total sediment (Figure 16).

[47] Our analysis yields valuable information concerning both Si cycle relevant processes and the marine Si budget. Our study indicates that more advanced particle dynamics models may significantly improve the simulation of the marine Si cycle. In nature, complex processes govern the coagulation and disaggregation of particles. The analysis proves quantitatively that an implementation of more realistic particle dynamics models (e.g., following *Kriest and Evans* [1999]) has a major improvement potential of the model. Our preliminary estimate of 1 g m^{-2} yr^{-1} for the clay deposition clearly was too low on the average. More realistic dust deposition fields from atmospheric models including dust mobilization modules as well as the simulation of turbidity currents and nepheloid layers including differential settling speed of the various clay size classes should be attempted in future models.

[48] According to the optimization, a revision to earlier marine Si budgets is suggested (Figure 9b). The marine throughput rate of silicon (input from continental weathering and output through sediment accumulation) as given by *Tréguer et al.* [1995] may have to be corrected downward by about 44% to a value of 3.1×10^{12} mol Si yr^{-1} This is consistent with investigations suggesting a higher opal retention rate at continental margins [*DeMaster*, 2002] as compared to the earlier estimate by *Tréguer et al.* [1995].

[49] Opal export production and deposition of opal onto the ocean floor could be reduced by 15–20% in the optimized version as compared to the control run, thus rendering also an improved lower opal particle flux rate through the water column (Figure 9b). The optimization procedure thus is capable of adjusting the model results in the direction of the bulk figures as given by *Tréguer et al.* [1995] and the considerably lower opal export production

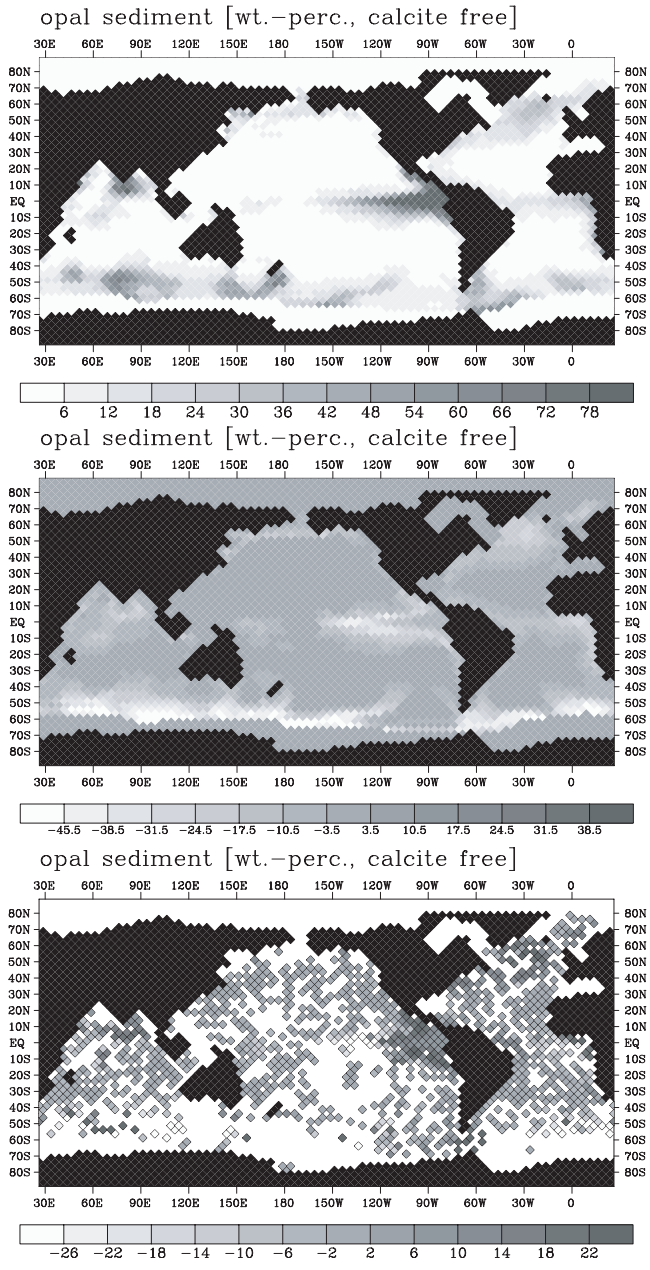

Figure 15. Opal sediment (weight-% on calcite free basis). (top) Optimized model run. (middle) Difference optimized run minus control run. (bottom) Difference in goodness of fit between optimized run and control run. See color version of this figure at back of this issue.

value of *Gnanadesikan* [1999] and thus farther away from the value as derived from inverse modeling by *Usbeck* [1999]. *Usbeck* [1999], on the other hand, could practically perfectly reproduce the $Si(OH)_4$ concentrations in the water column, which is not the case in our study. An upward correction of the export production value of 120×10^{12} mol Si yr^{-1} by *Tréguer et al.* [1995] in view of a potential underestimation of the Southern Ocean opal export production by *Pondaven et al.* [2000] would be supported by our

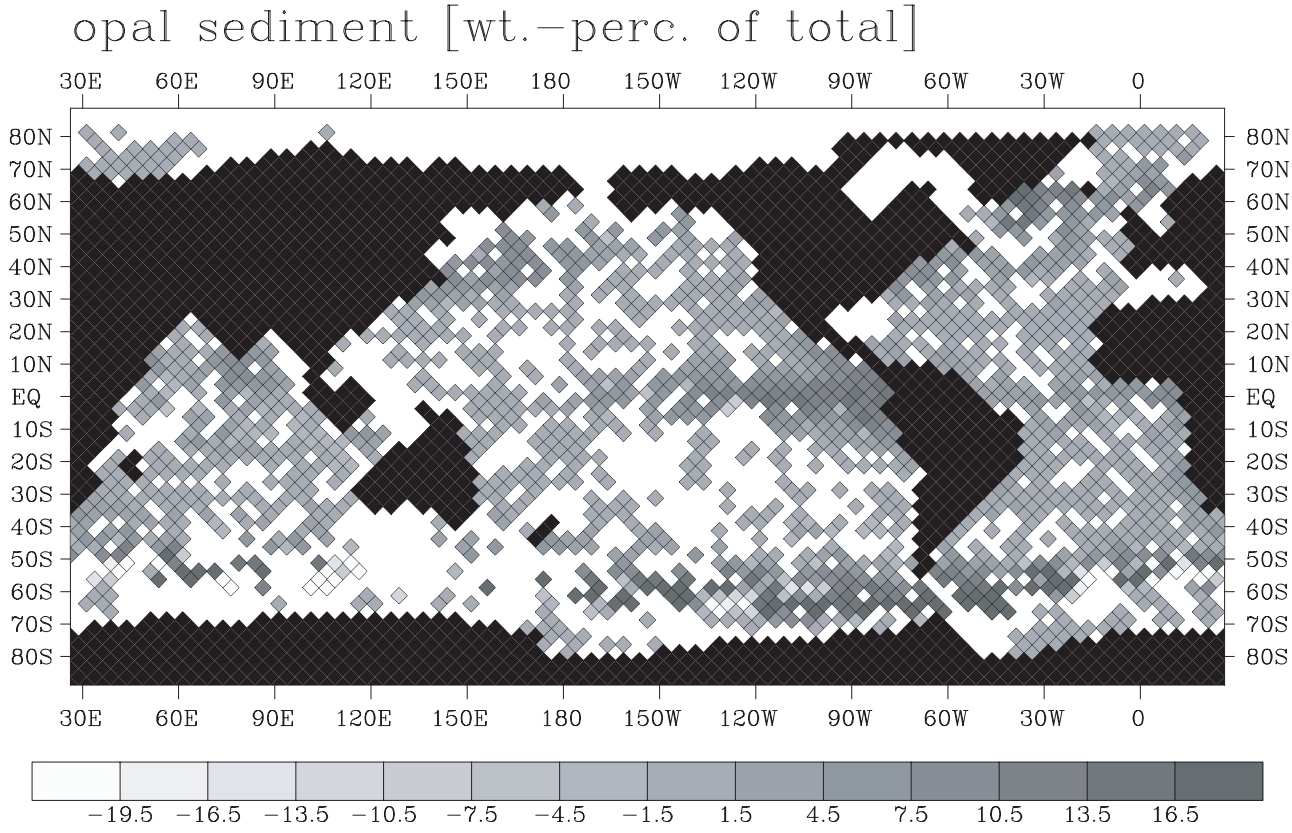

Figure 16. Opal sediment (weight-% relative to total sediment). Difference in goodness of fit between optimized run and control run.

study. It would be interesting to provide a marine Si budget from a purely inverse approach which should additionally include an early diagenesis module as well as a mechanistic particle aggregation part.

9. Conclusion

[50] The major remaining discrepancy between earlier Si cycle budget estimates and our result concerns the percentage of opal export production which is deposited onto the ocean bottom and the seeping of silicic acid from the sediment pore waters back into the open water column. In an earlier budget estimate by *Spencer* [1983], only about 7% of the Si export would reach the ocean floor and about 66% of the deposited matter would be re-released to the water column from the sediment porewaters. The deposition ratio in the study by *Tréguer et al.* [1995] amounts to about twice this value (16%), while in their study, 79% of the deposited opal is redissolved from the sediment. In our study a considerably larger fraction of the export production, 41%, arrives at the ocean bottom, of which 95% is re-released to the deep waters. The correct determination of the opal fluxes in the open water column is also crucial for a decision about which budget represents the quantitatively best estimate.

[51] In our study, we used a different methodology as employed for earlier estimates of the marine Si budget which relied on simpler box model approaches, regional extrapolations, and further assumptions such as estimates of the Si/C ratios in order to use, for example, POC productivities as analogues for opal productivities. We applied here a dynamical BOGCM and let the observations "speak" through this model. Though the biogeochemical formulations in our model are still based on empirical relationships, we can at least identify important processes and, within the present framework of the model and the observations available, place quantitative constraints on the processes. Of course, both the model and the database of measurements will have to be extended in future. Promising attempts to simulate the marine particle dynamics and the redissolution kinetics as well as the solubility of opal more mechanistically in BOGCMs have been initiated.

[52] **Acknowledgments.** This work was supported through the European Commission with grant MAS3-CT97-0141 (MAST-III Project "SINOPS"). Two very constructive reviewers helped to improve this manuscript.

References

Andersen, K. K., A. Armengaud, and C. Genthon, Atmospheric dust under glacial and interglacial conditions, *Geophys. Res. Lett.*, *25*, 2281–2284, 1998.

Antia, A. N., et al., Basin-wide particulate carbon flux in the Atlantic Ocean: Regional export patterns and potential for atmospheric CO_2 sequestration, *Global Biogeochem. Cycles*, *15*, 845–862, 2001.

Antia, N. J., A microbiological assay for biotin in seawater, *Can. J. Microbiol.*, *9*(3), 403, 1963.

Archer, D., and E. Maier-Reimer, Effect of deep-sea sedimentary calcite preservation on atmospheric CO_2 concentration, *Nature*, *367*, 260–263, 1994.

Archer, D., M. Lyle, K. Rodgers, and P. Froelich, What controls opal preservation in tropical deep-sea sediments?, *Paleoceanography*, *8*, 7–21, 1993.

Aumont, O., J. C. Orr, P. Monfray, G. Madec, and E. Maier-Reimer, Nutrient trapping in the equatorial Pacific: The ocean circulation solution, *Global Biogeochem. Cycles*, *13*, 351–369, 1999.

Bainbridge, A. E., *GEOSECS Atlantic Expedition*, vol. 1, *Hydrographic Data 1972–1973*, 121 pp., Natl. Sci. Found., Washington, D. C., 1981.

Behrenfeld, M. J., and P. G. Falkowski, Photosynthetic rates derived from satellite-based chlorophyll concentration, *Limnol. Oceanogr.*, *42*, 1–20, 1997.

Berelson, W. M., et al., Biogenic budgets of particle rain, benthic remineralization and sediment accumulation in the equatorial Pacific, *Deep Sea Res.*, *44*(9–10), 2251–2280, 1997.

Berger, W. H., K. Fischer, C. Lai, and G. Wu, Ocean productivity and organic carbon flux: I. Overview and maps of primary production and export production, *SIO Ref. 87-30*, 45 pp., Scripps Inst. of Oceanogr., Univ. of Calif., San Diego, La Jolla, 1987.

Berner, R. A., *Early Diagenesis: A Theoretical Approach*, Princeton Univ. Press, Princeton, N. J., 1980.

Broecker, W. S., and T.-H. Peng, Carbon cycle: 1985-Glacial to interglacial changes in the operation of the global carbon cycle, *Radiocarbon*, *28*, 309–327, 1986.

Broecker, W. S., S. Sutherland, W. Smethie, T.-H. Peng, and G. Östlund, Oceanic radiocarbon: Separation of the natural and bomb components, *Global Biogeochem. Cycles*, *9*, 263–288, 1995.

Brzezinski, M. A., The Si:C:N ratio of marine diatoms: Interspecific variability and the effect of some environmental variables, *J. Phycol.*, *21*, 347–357, 1985.

Buesseler, K. O., The decoupling of production and particulate export in the surface ocean, *Global Biogeochem. Cycles*, *12*, 297–310, 1998.

Craig, H., W. S. Broecker, and D. Spencer, *GEOSECS Pacific Expedition*, vol. 4, *Sections and Profiles*, 251 pp., Natl. Sci. Found., Washington, D. C., 1981.

DeMaster, D. J., The supply and accumulation of silica in the marine environment, *Geochim. Cosmochim. Acta*, *45*, 1715–1732, 1981.

DeMaster, D. J., The accumulation and cycling of biogenic silica in the Southern Ocean: Revisiting the marine silica budget, *Deep Sea Res., Part II*, *49*, 3155–3167, 2002.

DeMaster, D. J., R. B. Dunbar, L. I. Gordon, A. R. Leventer, J. M. Morrison, D. M. Nelson, C. A. Nittrouer, and W. O. Smith Jr., Cycling and accumulation of biogenic silica and organic matter in high latitude environments: The Ross Sea, *Oceanography*, *5*, 146–153, 1992.

DeMaster, D. J., W. O. Smith Jr., D. M. Nelson, and J. Y. Aller, Biogeochemical processes in Amazon shelf waters: Chemical distributions and uptake rates of silicon, carbon and nitrogen, *Cont. Shelf Res.*, *16*, 617–643, 1996a.

DeMaster, D. J., O. Ragueneau, and C. A. Nittrouer, Preservation efficiencies and accumulation rates for biogenic silica and C, N and P in high-latitude sediments: The Ross sea, *J. Geophys. Res.*, *101*, 18,501–18,518, 1996b.

Dittert, N., M. Diepenbroek, and H. Grobe, Scientific data must be made available to all, *Nature*, *414*, 393, 2001.

Dittert, N., M. Diepenbroek, C. Heinze, and O. Ragueneau, Managing (pale-)oceanographic data sets using the PANGAEA information system: The SINOPS example, *Comput. Geosci.*, *28*, 789–798, 2002.

Dixit, S., P. Van Cappellen, and A. J. van Bennekom, Processes controlling solubility of biogenic silica and porewater build-up of silicic acid in marine sediments, *Mar. Chem.*, *73*, 333–352, 2001.

Dugdale, R. C., and F. P. Wilkerson, Silicate regulation of new production in the eastern equatorial Pacific, *Nature*, *391*, 270–273, 1998.

Dugdale, R. C., F. P. Wilkerson, and H. J. Minas, The role of a silicate pump in driving new production, *Deep Sea Res.*, *42*, 697–719, 1995.

Dymond, J., and M. Lyle, Particle fluxes in the ocean and omplications for sources and prervation of ocean sediments, in *Material Fluxes on the Surface of the Earth*, pp. 125–142, Natl. Acad., Washington, D. C., 1994.

Edmond, J. M., and J. M. T. M. Gieskes, On the calculation of the degree of saturation of seawater with respect to calcium carbonate under in situ conditions, *Geochim. Cosmochim. Acta*, *34*, 1261–1291, 1970.

Gallinari, M., O. Ragueneau, L. Corrin, D. J. DeMaster, and P. Tréguer, The importance of water column processes on the dissolution properties of biogenic silica in deep sea sediments: I. Solubility, *Geochim. Cosmochi. Acta*, *66*, 2707–2717, 2002.

Gehlen, M., C. Heinze, E. Maier-Reimer, and C. I. Measures, Coupled Al-Si geochemistry in an ocean general circulation model: A tool for the validation of oceanic dust deposition?, *Global Biogeochem. Cycles*, *17*, 1028, doi:2001GB001549, 2003.

Geider, R. J., and J. LaRoche, The role of iron in phytoplankton photosynthesis, and the potential for iron-limitation of primary productivity in the sea, *Photosynth. Res.*, *39*, 275–301, 1994.

Gent, P., J. Willebrand, T. J. McDougall, and J. C. McWilliams, Parameterising eddy induced transports in ocean circulation models, *J. Phys. Oceanogr.*, *25*, 463–474, 1995.

Gnanadesikan, A., A global model of silicon cycling: Sensitivity to eddy parameterization and dissolution, *Global Biogeochem. Cycles*, *13*, 199–220, 1999.

Goering, J. J., D. M. Nelson, and J. A. Carter, Silicic uptake by natural populations of marine phytoplankton, *Deep Sea Res.*, *20*, 777–789, 1973.

Grill, E. V., and F. A. Richards, Nutrient regeneration from phytoplankton decomposing in seawater, *J. Mar. Res.*, *22*(1), 51–69, 1964.

Heinze, C., Towards the time-dependent modeling of sediment core data on a global basis, *Geophys. Res. Lett.*, *28*, 4211–4214, 2001.

Heinze, C., Assessing the importance of the Southern Ocean for natural atmospheric pCO_2 variations with a global biogeochemical general circulation model, *Deep Sea Res., Part II*, *49*, 3105–3125, 2002a.

Heinze, C., *Das Marine Sediment als Klimazeuge und Komponente des Klimasystems-Eine Modellstudie*, *Forschung und Wissen Ser.*, 124 pp., GCA-Verlag, Herdecke, Germany, 2002b.

Heinze, C., and E. Maier-Reimer, The Hamburg Oceanic Carbon Cycle Circulation Model Version "HAMOCC2s" for long time integrations, *Tech. Rep. 20*, 71 pp., Deutsches Klimarechenzentrum, Hamburg, Germany, 1999.

Heinze, C., E. Maier-Reimer, and K. Winn, Glacial pCO_2 reduction by the world ocean: Experiments with the Hamburg carbon cycle model, *Paleoceanography*, *6*, 395–430, 1991.

Heinze, C., E. Maier-Reimer, and P. Schlosser, Transient tracers in a global OGCM: Source functions and simulated distributions, *J. Geophys. Res.*, *103*, 15,903–15,922, 1998.

Heinze, C., E. Maier-Reimer, A. M. E. Winguth, and D. Archer, A global oceanic sediment model for longterm climate studies, *Global Biogeochem. Cycles*, *13*, 221–250, 1999.

Henderson, G. M., C. Heinze, R. F. Anderson, and A. M. E. Winguth, Global distribution of the ^{230}Th flux to ocean sediments constrained by GCM modelling, *Deep Sea Res., Part I*, *46*, 1861–1893, 1999.

Hofmann, M., D. A. Wolf-Gladrow, T. Takahashi, S. C. Sutherland, K. D. Six, and E. Maier-Reimer, Stable carbon isotope distribution of particulate organic matter in the ocean: A model study, *Mar. Chem.*, *72*, 131–150, 2000.

Honjo, S., J. Dymond, R. Collier, and S. J. Manganini, Export production of particles to the interior of equatorial Pacific Ocean during 1992 EqPaq experiment, *Deep Sea Res., Part II*, *42*, 831–870, 1995.

Ingle, S. E., Solubility of calcite in the ocean, *Mar. Chem.*, *3*, 301–319, 1975.

Kamatani, A., Regeneration of inorganic nutrients from diatom decomposition, *J. Oceanogr. Soc. Jpn.*, *25*, 63–74, 1969.

Koning, E., G.-J. Brummer, W. Van Raaphorst, A. J. Van Bennekom, W. Helder, and J. Van Yperen, Settling, dissolution and burial of biogenic silica in the sediments off Somalia (northwestern Indian Ocean), *Deep Sea Res., Part II*, *44*, 1341–1360, 1997.

Kriest, I., and G. T. Evans, Representing phytoplankton aggregates in biogeochemical models, *Deep Sea Res., Part I*, *46*, 1841–1859, 1999.

Lanczos, C., *Linear Differential Operators*, Van Nostrand Reinhold, New York, 1961.

Lawson, D. S., D. C. Hurd, and H. S. Pankratz, Silica dissolution rates of decomposing phytiplankton assemblages at various temperatures, *Am. J. Sci.*, *278*, 1373–1393, 1978.

Levitus, S., Climatological atlas of the world ocean, *Prof. Pap. 13*, Natl. Oceanic and Atmos. Admin., Silver Spring, Md., 1982.

Li, Y.-H., and S. Gregory, Diffusion of ions in sea water and in deep-sea sediments, *Geochim. Cosmochim. Acta*, *38*, 703–714, 1974.

Lorenz, S., B. Grieger, P. Helbig, and K. Herterich, Investigating the sensitivity of the Atmospheric General Circulation Model ECHAM 3 to paleoclimatic boundary conditions, *Geol. Rundschau*, *85*, 513–524, 1996.

Mahowald, N., K. Kohfeld, M. Hansson, Y. Balkanski, S. P. Harison, I. C. Prentice, M. Schulz, and H. Rodhe, Dust sources and deposition during the Last Glacial Maximum and current climate: A comparison of model results with paleodata from ice cores and marine sediments, *J. Geophys. Res.*, *104*, 15,895–15,916, 1999.

Maier-Reimer, E., Geochemical cycles in an ocean general circulation model: Preindustrial tracer distributions, *Global Biogeochem. Cycles*, *7*, 645–677, 1993.

Maier-Reimer, E., U. Mikolajewicz, and K. Hasselmann, Mean circulation of the Hamburg LSG OGCM and its sensitivity to the thermohaline surface forcing, *J. Phys. Oceanogr.*, *23*, 731–757, 1993.

Martin, J. H., G. A. Knauer, D. M. Karl, and W. W. Broenkow, VERTEX: Carbon cycling in the northeast Pacific, *Deep Sea Res.*, *34*, 267–285, 1987.

McManus, J. E., D. E. Hammond, W. M. Berelson, T. E. Kilgore, D. J. DeMaster, O. G. Ragueneau, and R. W. Collier, Early diagenesis of biogenic opal: Dissolution rates, kinetics, and paleoceanographic implications, *Deep Sea Res. Part II*, *42*, 871–903, 1995.

Michalopoulos, P., and R. C. Aller, Rapid clay mineral formation in Amazon Delta sediments: Reverse weathering and oceanic elemental fluxes, *Science*, *270*, 614–617, 1995.

Najjar, R. G., J. L. Sarmiento, and J. R. Toggweiler, Downward transport and fate organic matter in the ocean: Simulations with a general circulation model, *Global Biogeochem. Cycles*, *6*, 45–76, 1992.

Nelson, D. M., P. Tréguer, M. A. Brzezinski, A. Leynaert, and B. Quéguiner, Production and dissolution of biogenic silica in the ocean: Revised global estimates, comparison with regional data and relationship with biogenic sedimentation, *Global Biogeochem. Cycles*, *9*, 359–372, 1995.

Orr, J., Global Ocean Storage of Anthropogenic Carbon (GOSAC), EC Environ. and Clim. Programme final report, 116 p., Inst. Pierre Simon Laplace/CNRS, Guyancourt, France, 2001. (Available at http://www.ipsl.jussieu.fr/OCMIP/reports)

Paasche, E., Silicon and the ecology of Marine plankton diatoms: I. *Thalassiosira pseudonana* (Cyclotella nana) growth in a chemostat with silicate as limiting nutrient, *Mar. Biol.*, *19*, 117–126, 1973.

Parsons, T. R., and M. Takahashi, *Biological Oceanographic Processes*, 186 pp., Pergamon, New York, 1973.

Pondaven, P., O. Ragueneau, P. Tréguer, A. Hauvespre, L. Dezileau, and J. L. Reyss, Resolving the "opal paradox" in the Southern Ocean, *Nature*, *405*, 168–172, 2000.

Press, W. H., S. A. Teukolsky, W. T. Vetterling, and B. P. Flannery, *Numerical Recipes in FORTRAN*, 2nd ed., 963 pp., Cambridge Univ. Press, New York, 1992.

Rabouille, C., J.-F. Gaillard, P. Tréguer, and M.-A. Vincendeau, Biogenic silica recycling in surficial sediments across the Polar Front Zone of the Southern Ocean (Indian Sector), *Deep Sea Res., Part II*, *44*, 1151–1176, 1997.

Ragueneau, O., A. Leynaert, P. Tréguer, D. J. DeMaster, and R. F. Anderson, Opal studied as a marker of paleoproductivity, *Eos Trans. AGU*, *77*(49), 491–493, 1996.

Ragueneau, O., et al., A review of the Si cycle in the modern ocean: recent progress and missing gaps in the application of biogenic opal as a paleoproductivity proxy, *Global Planet. Change*, *26*, 317–365, 2000.

Ragueneau, O., et al., The benthic silica cycle in the Northeast Atlantic: annual mass balance, seasonality, and importance of non-steady state processes for the early diagenesis of biogenic opal in deep-sea sediments, *Prog. Oceanogr.*, *50*, 171–200, 2001.

Rickert, D., Dissolution kinetics of biogenic silica in marine environments, *Ber. Polarforschung., 351*, 211 pp., Alfred-Wegener-Inst. für Polar- und Meeresforschung, Bremerhaven, Germany, 2000.

Sayles, F. L., W. G. Deuser, J. E. Goudreau, W. H. Dickinson, T. D. Jickells, and P. King, The benthic cycle of biogenic opal at the Bermuda Atlantic Time Series site, *Deep Sea Res., Part I*, *43*, 383–409, 1996.

Schneider, R. R., P. J. Müller, and M. Zabel, Biogenic opal in the eastern south Atlantic: patterns of surface water productivity, sedimentary accumulation and bethic $Si(OH)_4$ fluxes in relation to oceanic and fluvial nutrient supply, in *OPALEO: On the Use of Opal as a Paleo-Productivity Proxy: Minutes of the First Workshop*, edited by O. Ragueneau, A. Leynaert, and P. Tréguer, pp. 98–103, Inst. Univ. Eur. de la Mer, Univ. de Bretagne Occidentale, Brest, France, 1996.

Scholten, J. C., J. Fietzke, S. Vogler, M. M. Rutgers van der Loeff, A. Mangini, W. Koeve, J. Waniek, P. Stoffers, A. Antia, and J. Kuss, Trapping efficiencies of sediment traps from the deep Eastern North Atlantic: The ^{230}Th calibration, *Deep Sea Res., Part II*, *48*, 2383–2408, 2001.

Suess, E., Particulate organic carbon flux in the oceans-Surface productivity and oxygen utilization, *Nature*, *288*, 260–263, 1980.

Six, K., and E. Maier-Reimer, Effects of plankton dynamics on seasonal carbon fluxes in an ocean general circulation model, *Global Biogeochem. Cycles*, *10*, 559–583, 1996.

Spencer, C. P., Marien biogeochemistry of silicon, in *Silicon Geochemistry and Biogeochemistry*, edited by S. R. Aston, pp. 101–141, Academic, San Diego, Calif., 1983.

Thomas, W. H., and A. N. Dodson, Effects of phosphate concentration on cell division rates and yield of a tropical oceanic diatom, *Biol. Bull.*, *134*(1), 199–208, 1968.

Tréguer, P., D. M. Nelson, A. J. Van Bennekom, D. J. DeMaster, A. Leynaert, and B. Quéguiner, The balance of silica in the world ocean: A re-estimate, *Science*, *268*, 375–379, 1995.

Ullman, W. J., and R. C. Aller, Diffusion coefficients in nearshore marine environments, *Limnol. Oceanogr.*, *27*, 552–556, 1982.

Usbeck, R., Modeling of marine biogeochemical cycles with an emphasis on vertical particle fluxes, *Ber. Polarforschung, 332*, 105 pp., 1999.

Van Bennekom, A. J., G. W. Berger, S. J. van der Gaast, and R. T. P. de Vries, Primary productivity and the silica cycle in the Southern Ocean (Atlantic sector), *Paleogeogr. Paleoclimatol. Paleoecol.*, *67*, 19–30, 1988.

Van Cappellen, P., and L. Qiu, Biogenic silica dissolution in sediments of the Southern Ocean: I. Solubility, *Deep Sea Res., Part II*, *44*, 1109–1128, 1997.

Volk, T., and M. Hoffert, Ocean carbon pumps: Analysis of relative strengths and efficiencies in ocean-driven pCO_2 changes, in *The Carbon Cycle and Atmospheric CO_2: Natural Variations Archean to Present*, *Geophys. Monogr. Ser.*, *32*, edited by E. T. Sundquist and W. S. Broecker, pp. 99–110, AGU, Washington, D. C., 1985.

Winguth, A. M. E., D. Archer, J.-C. Duplessy, E. Maier-Reimer, and U. Mikolajewicz, Sensitivity of paleonutrient tracer distributions and deep sea circulation to glacial boundary conditions, *Paleoceanography*, *14*, 304–323, 1999.

Woodruff, S. D., R. J. Slurz, R. L. Jenne, and P. M. Steurer, A comprehensive ocean-atmosphere data set, *Bull. Am. Meteorol. Soc.*, *68*, 1239–1250, 1987.

Wunsch, C., Tracer inverse problems, in *Oceanic Circulation Models: Combinig Data and Dynamics*, edited by D. L. T. Anderson and J. Willebrand, pp. 1–77, Kluwer Acad., Norwell, Mass., 1989.

Yu, E.-F., R. Francois, M. P. Bacon, S. Honjo, A. P. Fleer, S. J. Manganini, M. M. Rutgers van der Loeff, and V. Ittekot, Trapping efficiency of bottom-tethered sediment traps estimated from the intercepted fluxes of ^{230}Th and ^{231}Pa, *Deep Sea Res., Part I*, *48*, 865–889, 2001.

N. Dittert and O. Ragueneau, Unité Mixte de Recherche 6539-IUEM, Technopole Brest-Iroise, Place Nicolas Copernic, F-29280 Plouzané, France. (nicolas.dittert@univ-brest.fr; olivier.ragueneau@univ.brest.fr)

C. Heinze, A. Hupe, and E. Maier-Reimer, National Model and Data Group, Max Planck Institute of Meteorology, Bundesstrasse 55, D-20146 Hamburg, Germany. (heinze@dkrz.de; hupe@dkrz.de; maier-reimer@dkrz.de)

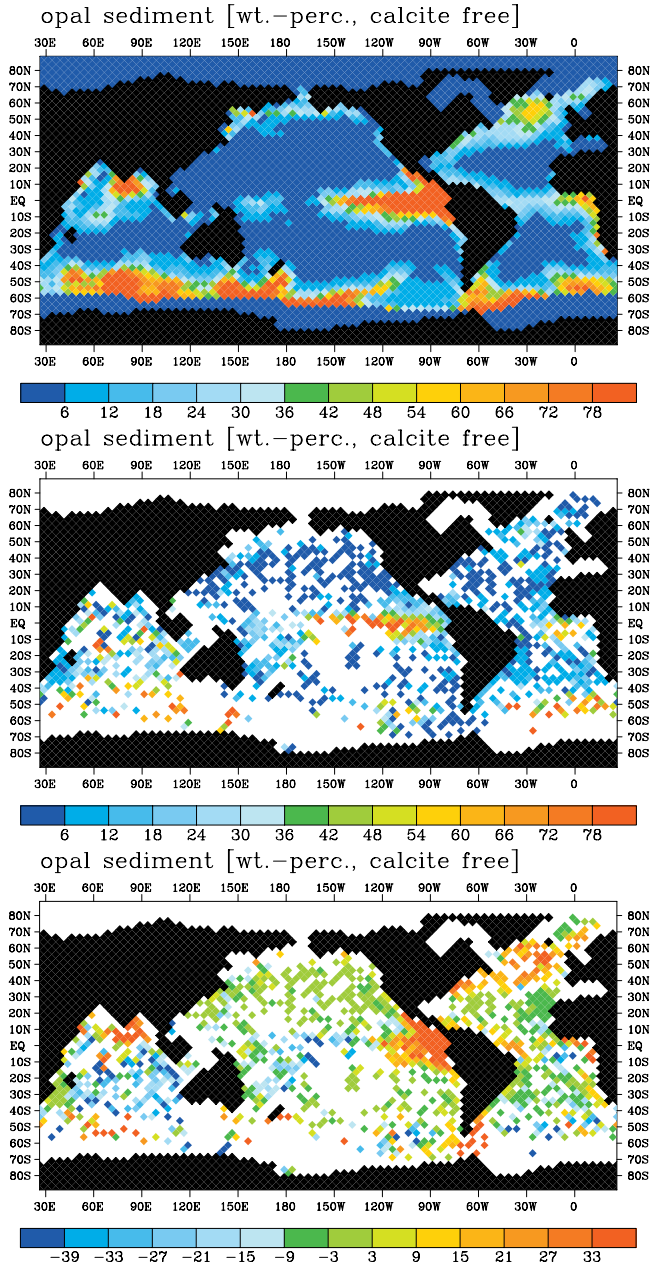

Figure 5. Opal sediment (weight-% on calcite free basis). (top) Model (control run). (middle) Observations (SINOPS data compilation http://www.pangaea.de/PangaVista?query=sinops). (bottom) Difference model – observations. (Comparison is based on averages over the entire bioturbated zone.)

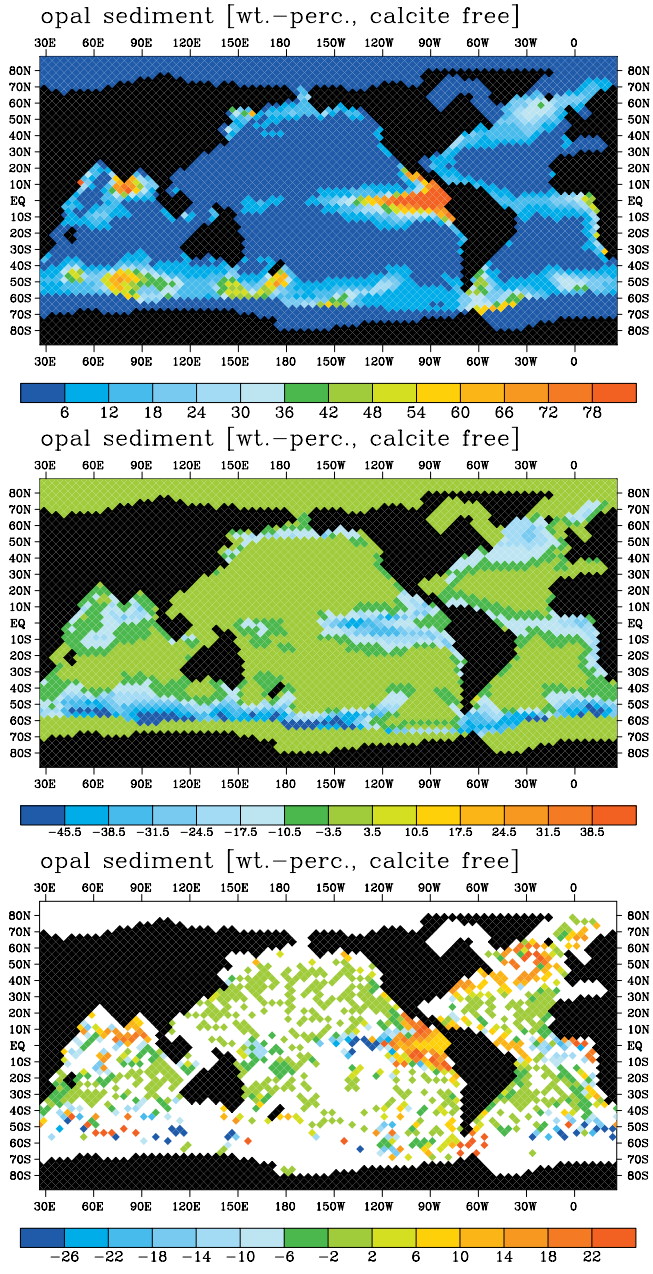

Figure 15. Opal sediment (weight-% on calcite free basis). (top) Optimized model run. (middle) Difference optimized run minus control run. (bottom) Difference in goodness of fit between optimized run and control run.